11. V. I. Prokhorenko *et al.*, *Science* **313**, 1257 (2006).
12. J. Savolainen *et al.*, *Proc. Natl. Acad. Sci. U.S.A.* **105**, 7641 (2008).
13. I. Otake, S. S. Kano, A. Wada, *J. Chem. Phys.* **124**, 014501 (2006).
14. C. Daniel *et al.*, *Science* **299**, 536 (2003).
15. M. P. A. Branderhorst *et al.*, *Science* **320**, 638 (2008).
16. R. A. Bartels, M. M. Murnane, H. C. Kapteyn, I. Christov, H. Rabitz, *Phys. Rev. A* **70**, 043404 (2004).
17. D. Cardoza, C. Trallero-Herrero, F. Langhojer, H. Rabitz, T. Weinacht, *J. Chem. Phys.* **122**, 124306 (2005).
18. M. A. Montgomery, R. R. Meglen, N. H. Damrauer, *J. Phys. Chem. A* **110**, 6391 (2006).
19. M. A. Montgomery, R. R. Meglen, N. H. Damrauer, *J. Phys. Chem. A* **111**, 5126 (2007).
20. J. L. White, B. J. Pearson, P. H. Bucksbaum, *J. Phys. At. Mol. Opt. Phys.* **37**, L399 (2004).
21. $2G_2$-m-Per is a second-generation dendrimer with two monodendrons on meta positions and an ethynylene perylene trap.
22. Z. H. Peng, J. S. Melinger, V. Kleiman, *Photosynth. Res.* **87**, 115 (2006).
23. E. Atas, Z. H. Peng, V. D. Kleiman, *J. Phys. Chem. B* **109**, 13553 (2005).
24. Z. H. Peng, Y. C. Pan, B. B. Xu, J. H. Zhang, *J. Am. Chem. Soc.* **122**, 6619 (2000).
25. Materials and methods are available as supporting material on *Science* Online.
26. S. F. Swallen, R. Kopelman, J. S. Moore, C. Devadoss, *J. Mol. Struct.* **486**, 585 (1999).
27. D. Meshulach, Y. Silberberg, *Nature* **396**, 239 (1998).
28. D. Meshulach, D. Yelin, Y. Silberberg, *Opt. Commun.* **138**, 345 (1997).
29. T. Brixner, N. H. Damrauer, B. Kiefer, G. Gerber, *J. Chem. Phys.* **118**, 3692 (2003).
30. M. H. B. Schmidt, G. Stobrawa, T. Feurer, LAB2-A virtual femtosecond laser lab, www.lab2.de.
31. L. G. C. Rego, L. F. Santos, V. S. Batista, *Annu. Rev. Phys. Chem.* **60**, 293 (2009).
32. D. Meshulach, Y. Silberberg, *Phys. Rev. A* **60**, 1287 (1999).
33. M. A. Montgomery, N. H. Damrauer, *J. Phys. Chem. A* **111**, 1426 (2007).
34. V. D. Kleiman, S. M. Arrivo, J. S. Melinger, E. J. Heilweil, *Chem. Phys.* **233**, 207 (1998).
35. T. Brixner, N. H. Damrauer, P. Niklaus, G. Gerber, *Nature* **414**, 57 (2001).
36. J. P. Ogilvie, K. J. Kubarych, A. Alexandrou, M. Joffre, *Opt. Lett.* **30**, 911 (2005).

37. This work was supported by the NSF, CHE-0239120.

Supporting Online Material

www.sciencemag.org/cgi/content/full/326/5950/263/DC1
Materials and Methods
SOM Text
Figs. S1 to S11
References

19 May 2009; accepted 31 August 2009
10.1126/science.1176524

Repetitive Readout of a Single Electronic Spin via Quantum Logic with Nuclear Spin Ancillae

L. Jiang,[1]*† J. S. Hodges,[1,2]* J. R. Maze,[1]* P. Maurer,[1] J. M. Taylor,[3]‡ D. G. Cory,[2] P. R. Hemmer,[4] R. L. Walsworth,[1,5] A. Yacoby,[1] A. S. Zibrov,[1] M. D. Lukin[1]§

Robust measurement of single quantum bits plays a key role in the realization of quantum computation and communication as well as in quantum metrology and sensing. We have implemented a method for the improved readout of single electronic spin qubits in solid-state systems. The method makes use of quantum logic operations on a system consisting of a single electronic spin and several proximal nuclear spin ancillae in order to repetitively readout the state of the electronic spin. Using coherent manipulation of a single nitrogen vacancy center in room-temperature diamond, full quantum control of an electronic-nuclear system consisting of up to three spins was achieved. We took advantage of a single nuclear-spin memory in order to obtain a 10-fold enhancement in the signal amplitude of the electronic spin readout. We also present a two-level, concatenated procedure to improve the readout by use of a pair of nuclear spin ancillae, an important step toward the realization of robust quantum information processors using electronic- and nuclear-spin qubits. Our technique can be used to improve the sensitivity and speed of spin-based nanoscale diamond magnetometers.

Efforts have recently been directed toward the manipulation of several qubits in quantum systems, ranging from isolated atoms and ions to solid-state quantum bits (*1*, *2*). These small-scale quantum systems have been successfully used for proof-of-concept demonstrations of simple quantum algorithms (*3*–*6*). In addition, they can be used for potentially important practical applications in areas such as quantum metrology (*1*). For example, techniques involving quantum logic operations on several trapped ions have been applied to develop an improved ion state readout scheme, resulting in a new class of atomic clocks (*7*, *8*). We developed a similar technique to enhance the readout of a single electronic spin in the solid state.

Our method makes use of quantum logic between a single electronic spin and nuclear spin qubits in its local environment for repetitive readout. Although such nuclear spins are generally the source of unwanted decoherence in the solid state, recent theoretical (*9*–*11*) and experimental (*12*–*18*) work has demonstrated that when properly controlled, the nuclear environment can become a very useful resource, in particular for long-term quantum memory.

Our experimental demonstration makes use of a single negatively charged nitrogen-vacancy (NV) center in diamond. The electronic ground state of this defect is an electronic spin triplet (with spin $S = 1$) and is a good candidate for a logic qubit on account of its remarkably long coherence times (*19*) and fast spin manipulation by use of microwave fields (*20*). Furthermore, the center can be optically spin-polarized and measured by combining confocal microscopy techniques with spin-selective rates of fluorescence (*12*). In practice, the NV spin readout under ambient room-temperature conditions is far from perfect. This is because laser radiation at 532 nm for readout repolarizes the electronic spin before a sufficient number of photons can be scattered for the state to be reliably determined.

Our approach is to correlate the electronic-spin logic qubit with nearby nuclear spins (*21*), which are relatively unperturbed by the optical readout, before the measurement process (*22*). Specifically, we used one or more ^{13}C nuclei (with nuclear spin $I = 1/2$) nuclear spins in the diamond lattice, coupled to the NV electronic spin via a hyperfine interaction, as memory ancillae qubits. For example, a single ^{13}C nuclear spin has eigenstates $|\uparrow\rangle_{n1}$ (aligned) or $|\downarrow\rangle_{n1}$ (anti-aligned) with the local magnetic field. The composite electronic-nuclear system was first prepared in a fiducial state, $|0\rangle_e\,|\downarrow\rangle_{n1}$, by using a sequence of optical, microwave, and radiofrequency (RF) pulses. Next, the electronic spin was prepared in an arbitrary state $|\Psi\rangle_e = \alpha|0\rangle_e + \beta|1\rangle_e$, where $|0,1\rangle_e$ denote electronic state with projected spin momentum m_S (m_S) = 0, 1. Before readout, we performed a sequence of gate operations resulting in the entangled electron-nuclear state $|\Psi\rangle_e\,|\downarrow\rangle_{n1} \rightarrow \alpha|0\rangle_e\,|\downarrow\rangle_{n1} + \beta|1\rangle_e\,|\uparrow\rangle_{n1}$. The optical measurement process projects this state into either $|0\rangle_e\,|\downarrow\rangle_{n1}$ or $|1\rangle_e\,|\uparrow\rangle_{n1}$. When optically excited, these two states fluoresce at different rates dependent on the value of m_S. Within a typical measurement period, less than one photon was counted before the electron spin was repolarized to $|0\rangle_e$, which indicates that the uncertainty of the electronic spin-state measurement is quite large.

The nuclear spin can thus reveal the former electronic state because of the correlations established before the electronic spin was reset. To achieve this repetitive readout, we performed a controlled-not operation, which mapped $|0\rangle_e\,|\downarrow\rangle_{n1} \rightarrow |0\rangle_e\,|\downarrow\rangle_{n1}$ and $|0\rangle_e\,|\uparrow\rangle_{n1} \rightarrow |1\rangle_e\,|\uparrow\rangle_{n1}$, and repeated the

[1]Department of Physics, Harvard University, Cambridge, MA 02138, USA. [2]Department of Nuclear Science and Engineering, Massachusetts Institute of Technology (MIT), Cambridge, MA 02139, USA. [3]Department of Physics, MIT, Cambridge, MA 02139, USA. [4]Department of Electrical and Computer Engineering, Texas A&M University, College Station, TX 77843, USA. [5]Harvard-Smithsonian Center for Astrophysics, Cambridge, MA 02138, USA.

*These authors contributed equally to this work.
†Present address: Institute for Quantum Information, California Institute of Technology, Pasadena, CA 91125, USA.
‡Present address: Joint Quantum Institute, University of Maryland, College Park, MD 20742, USA.
§To whom correspondence should be addressed. E-mail: lukin@fas.harvard.edu

optical measurement. Fluorescence counting of these two states can be added to prior measurements so as to decrease the uncertainty for electronic spin-state discrimination. If optical readout does not destroy the orientation of the nuclear spin, the uncertainty in the determination of the electronic spin can be reduced via repetitive measurements. In this way, the overall signal-to-noise of the measurement process of our logic qubit can be increased. After multiple readout cycles and many quantum logic operations, the nuclear spin orientation will finally be destroyed. However, it is possible to further improve the readout scheme by using a pair of ancillary nuclear spins and imprinting the electronic state into a Greenberger-Horne-Zeilinger (GHZ)–like state: $|\Psi\rangle_e|\downarrow\rangle_{n1}|\downarrow\rangle_{n2} \rightarrow \alpha|0\rangle_e|\downarrow\rangle_{n1}|\downarrow\rangle_{n2} + \beta|1\rangle_e|\uparrow\rangle_{n1}|\uparrow\rangle_{n2}$. In such a case, the state of the first nuclear spin after repetitive readout sequences can be periodically "refreshed" by using the information stored within the second nuclear spin. These schemes are closely related to a quantum nondemolition (QND) measurement (*23*, *24*) because the nuclear spin-population operators $\hat{I}_z^{n1,n2}$ do not evolve throughout the electronic-spin readout and constitute "good" QND observables. Although imperfect, optical NV electronic spin detection precludes an ideal QND measurement, our scheme nevertheless allows substantial improvement in the spin readout.

To implement the repetitive readout technique, we used a single NV center in diamond coupled to nearby ^{13}C nuclear spins. These nuclear spins can be polarized and fully controlled and provide a robust quantum memory, even in the presence of optical radiation necessary for electronic spin-state readout (*13*, *22*). This is achieved through a combination of optical, microwave, and RF fields (Fig. 1) and is discussed in (*25*).

To control a single nuclear spin, we chose a NV center with a well-resolved ^{13}C hyperfine coupling near 14 MHz. The degeneracy of the $|m_S = \pm 1\rangle_e$ spin states was lifted by applying a $B_0 = 30$ gauss magnetic field along the NV axis. Under these conditions, the transitions of the electronic spin (**e**) within the subspace of $\{|0\rangle_e, |1\rangle_e\}$ can be selectively addressed, conditioned on a certain nuclear state. The model Hamiltonian for this system (Fig. 1A) is

$$H = (\Delta + \gamma_e B_0)\hat{S}_z + \gamma_C B_0 \hat{I}_z^{n1} + A\hat{S}_z\hat{I}_z^{n1} \quad (1)$$

where $\Delta = 2\pi \times 2.87$ GHz is the zero field splitting, A is the hyperfine interaction, and γ_e and γ_C are the electronic- and nuclear-spin gyromagnetic ratios. $\hat{S}_z = \frac{1}{2}\hat{\mathbf{1}} + \hat{S}_z$ is a pseudo-spin one-half operator for the electronic spin subspace, $\hat{\mathbf{1}}$ is the identity matrix, and $\hat{I}_z^{n1}$ and $\hat{S}_z$ are the spin-1/2 angular momentum operators. Coherent oscillations between the $|0\rangle_e$ and $|1\rangle_e$ states, conditioned on a single proximal nuclear spin ($\mathbf{n}_1$) in $|\downarrow\rangle_{n1}$ (or $|\uparrow\rangle_{n1}$), were selectively driven by the microwave field MW1 (or MW2). To control nuclear spin $\mathbf{n}_1$, a resonantly tuned RF field to address the levels $|1\rangle_e|\downarrow\rangle_{n1}$ and $|1\rangle_e|\uparrow\rangle_{n1}$, which are energetically separated because of the hyperfine interaction (Fig. 1A), was used. After the initialization of spin **e**, spin $\mathbf{n}_1$ was polarized by applying MW1 and RF π pulses, which transfers the polarization from spin **e** to spin $\mathbf{n}_1$. Rabi oscillations of spin $\mathbf{n}_1$ were demonstrated (Fig. 1E) by preparing spin **e** in the $|1\rangle_e$ state irrespective of the state of spin $\mathbf{n}_1$ (by using MW1 and MW2 π-pulses) and increasing the RF pulse length. These data indicate that we can achieve spin $\mathbf{n}_1$ preparation (polarization) and readout with combined fidelity $F \equiv \langle\downarrow|\rho'|\downarrow\rangle \geq 75\%$, where ρ' is the reduced density operator for spin $\mathbf{n}_1$.

We now describe the repetitive readout technique. As illustrated in Fig. 1D, the direct readout of electronic spin is imperfect. We define n^0 and n^1 as the total number of photons detected for the $|0\rangle_e$ and $|1\rangle_e$ states, respectively, during a single measurement interval. The signal is defined as the difference in average counts between the two spin states: $A_0 = n^0 - n^1 \approx 0.005$ (Fig. 1D). Experimentally, photon shot-noise dominated the fluctuations in the counts. Because of this shot

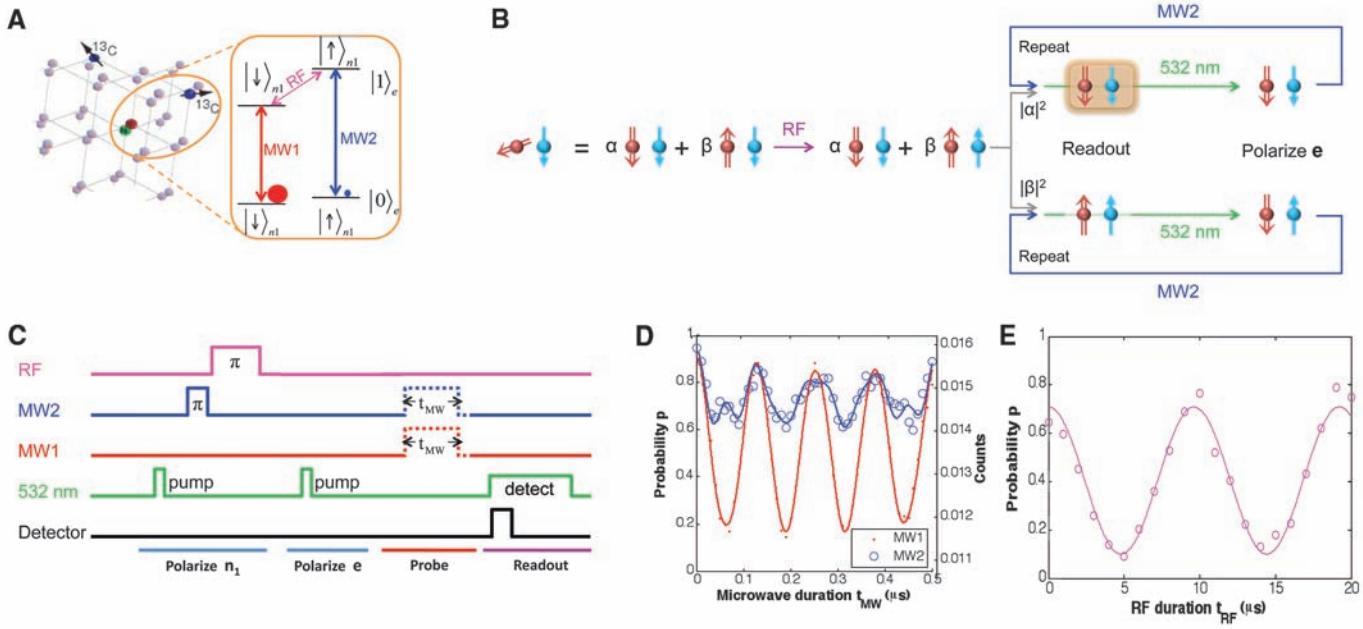

Fig. 1. Repetitive readout of an electronic spin. (**A**) Illustration of the NV center and its proximal ^{13}C nuclear spins. (Inset) Energy levels of the coupled spin system formed by the NV electronic spin (**e**) and the first proximal ^{13}C nuclear spin ($\mathbf{n}_1$). With a static magnetic field applied along the NV axis, spin $\mathbf{n}_1$ keeps the same quantization axis when spin **e** is $|0\rangle_e$ or $|1\rangle_e$ (*25*). When spin $\mathbf{n}_1$ is $|\downarrow\rangle_{n1}$ (or $|\uparrow\rangle_{n1}$), the microwave field MW1 (or MW2) resonantly drives spin **e** between $|0\rangle_e$ and $|1\rangle_e$, which can implement the $C_{n1}NOT_e$ gate. When spin **e** is $|1\rangle_e$, the RF field resonantly drives spin $\mathbf{n}_1$ between $|\downarrow\rangle_{n1}$ and $|\uparrow\rangle_{n1}$, which can implement the C_eNOT_{n1} gate. (**B**) Illustration of repetitive readout. The red down arrow represents the electronic spin state $|0\rangle_e$, the red up arrow represents the electronic spin state $|1\rangle_e$, the blue down arrow represents the nuclear spin state $|\downarrow\rangle_{n1}$, and the blue up arrow represents the nuclear spin state $|\uparrow\rangle_{n1}$. (**C**) Experimental pulse sequences that polarize spin $\mathbf{n}_1$ to $|\downarrow\rangle_{n1}$ and spin **e** to $|0\rangle_e$, followed by various probe operations, before fluorescence readout of spin **e**. (**D**) Measured electronic spin Rabi oscillations driven by MW1 and MW2 fields for polarized spin $\mathbf{n}_1$. The small wiggles for MW2 are due to off-resonant driving of the majority population in the $|\downarrow\rangle_{n1}$ state. The data are in agreement for finite detunings and microwave power (solid curves). The right vertical axis shows the average counts for a single readout. The left vertical axis shows the probability in the $|0\rangle_e$ state, obtained from the average counts (*25*). (**E**) Measured nuclear spin Rabi oscillation driven by the RF field.

noise and the low average count ($n^0 \approx 0.016$), we needed to average over $N \sim 10^5$ experimental runs in order to obtain the data in Fig. 1D.

To improve the signal, we used two spins: **e** and $\mathbf{n}_1$. Both spins were first polarized to the initial state $|0\rangle_e |\downarrow\rangle_{n1}$. Next, we performed a unitary operation $U(t)$, which prepares the superposition state $|\Psi_1\rangle = (\alpha|0\rangle_e + \beta|1\rangle_e) |\downarrow\rangle_{n1}$ that we wanted to measure. Instead of immediately reading out the electronic spin, we use a controlled-not gate ($C_e NOT_{n1}$, achieved with an RF π pulse) to correlate spin **e** with spin $\mathbf{n}_1$ (Fig. 2A). We then optically readout/pumped spin **e**, leaving the spin system in the post-readout state: $\rho_{post} = |0\rangle\langle 0|_e \otimes (|\alpha|^2 |\downarrow\rangle\langle\downarrow| + |\beta|^2 |\uparrow\rangle\langle\uparrow|)_{n1}$. The state of spin $\mathbf{n}_1$ via the electronic spin **e** by performing a controlled-not operation ($C_{n1} NOT_e$, achieved with an MW1 or MW2 π pulse) was then readout. This completes a one-step readout of spin $\mathbf{n}_1$, which can be repeated.

As a direct illustration of the enhanced readout technique, Fig. 2C shows the accumulated signal for Rabi oscillations of the electronic spin obtained by adding M subsequent repetitive readouts for each experimental run. This procedure results in a 10-fold enhancement of spin signal amplitude.

In order to further quantify the performance of this technique, the noise added with each additional repetitive readout must be considered. The repetitive readout spin signal is defined as a weighted sum of difference counts A_m associated with mth readout: $S_w(M) = \sum_{m=1}^{M} w_m A_m$. The average values of A_m were determined experimentally by measuring the difference in average counts associated with Rabi oscillations for each mth repeated readout. The w_m allowed us to weight the contribution of each repetitive readout to the overall signal. The noise corresponding to the repetitive readout signal is $\Delta S_w(M) = \sqrt{\sum_{m=1}^{M} w_m^2 \sigma_m^2}$. Here, σ_m is the uncertainty of the measurement of A_m. Experimentally, this uncertainty was found to be independent of m.

The signal-to-noise figure of merit is defined as $SNR\ (M) = S_w(M)/\Delta S_w(M)$. The w_m weights were chosen by noting that the larger values of A_m allow us to extract more information given the fixed uncertainty of each measurement, and we should emphasize these readouts more. As proven in (*25*), the optimal choice of weights corresponds to $w_m = |A_m|/\sigma_m^2$, and the optimized SNR is given by

$$\mathrm{SNR}_{opt}(M) = \sqrt{\sum_{m=1}^{M} \left|\frac{A_m}{\sigma_m}\right|^2} \qquad (2)$$

In the ideal QND case, each repetitive readout would yield the same $|A_m|$, and the SNR would scale with $\sqrt{M}$. For our experiment, the SNR saturates (Fig. 2E) because of the decay of the normalized amplitudes (Fig. 3D). Nevertheless, the experimental data shown in Fig. 2E indicate the enhancement of SNR by more than 220%.

In assessing this result, it is noted that various imperfections can affect the repetitive readout, which leads to the imperfect first readout $|A_1|/|A_0| < 1$, the sharp decrease in $|A_2|$, and the subsequent exponential reduction $|A_m| = |A_2|\eta^{(m-2)}$, with $\eta \approx 0.95$. These behaviors can be attributed to three major imperfections (*25*): (i) errors from microwave pulses (about 7% error probability for each π pulse), (ii) imperfect optical pumping of the electronic spin after each readout; and most substantially (iii) the depolarization of the nuclear-spin memory under optical illumination.

To quantify the latter process, we studied the decay times for ^{13}C nuclear spins in the presence of optical illumination. For an illumination time t_L longer than 1 μs, the nuclear spin polarization decays exponentially, with a characteristic time of $\tau_{n1} = 13\ (1)$ μs (Fig. 3B). Because τ_{n1} is much longer than the time for optical readout and optical spin polarization of the NV electronic spin (350 ns), repetitive readout of **e** is possible. [In the absence of optical illumination, the ^{13}C nuclear spin decay times are >>1 ms (*12*, *13*).] Despite the relatively long τ_{n1}, after many cycles the nuclear spin depolarizes. This degrades the repetitive optical readout for larger m, yielding the overall exponential decay in the amplitude $|A_m|$ with increasing m (*25*).

As an indication of how this limit can be circumvented, the use of two ancillary nuclear spins

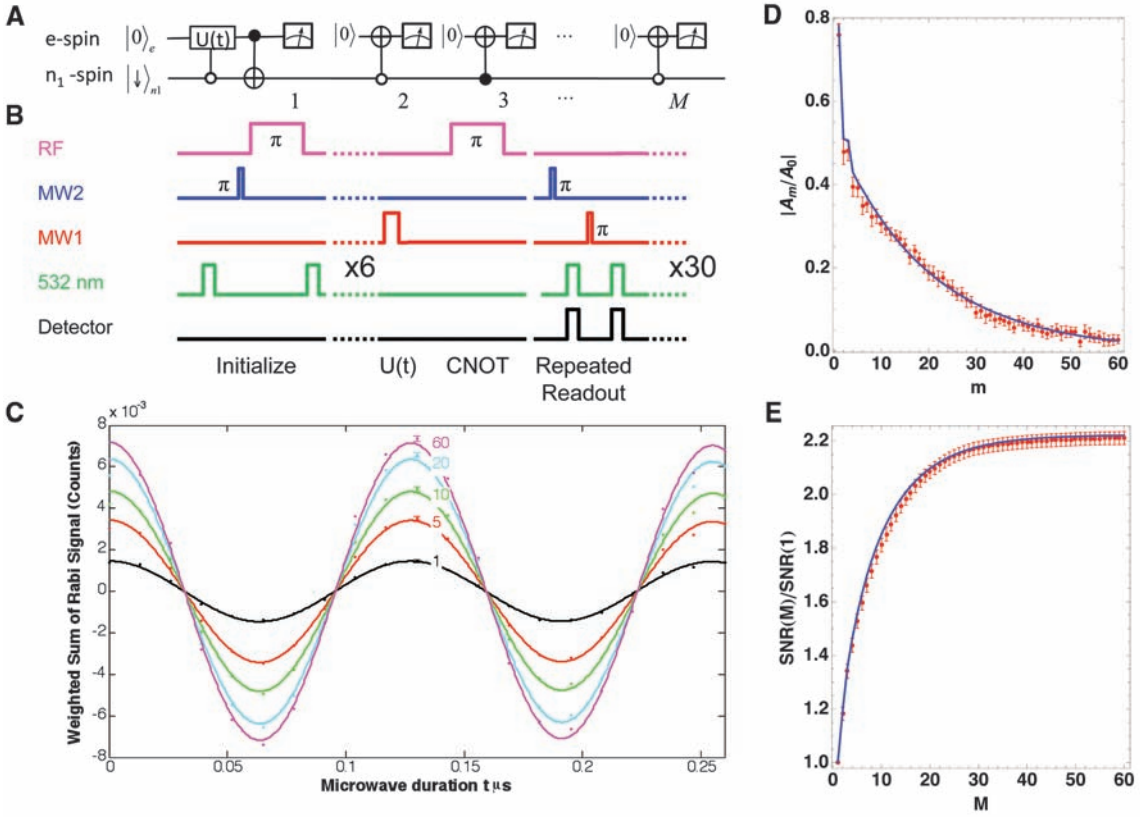

Fig. 2. Realization of repetitive readout. (**A**) Quantum circuit for M-step repetitive readout scheme assisted by spin $\mathbf{n}_1$. (**B**) Operations and pulse sequences for $M = 60$. The initial state $|0\rangle_e |\downarrow\rangle_{n1}$ is prepared with a six-step pumping of spins **e** and $\mathbf{n}_1$. The MW1 pulse of duration t induces the Rabi rotation $U(t)$ of spin **e**, whose parity information is imprinted to spin $\mathbf{n}_1$ with an RF π pulse (the $C_e NOT_{n1}$ gate). After fluorescence readout of spin **e**, $(M - 1)$–repetitive readouts of spin $\mathbf{n}_1$ are performed by means of MW1 or MW2 π pulses ($C_{n1} NOT_e$ gates) followed by fluorescence readout. The $m = 1$ readout is not preceded by a MW1 pulse. (**C**) Cumulative signal obtained from repetitive readout measurements, summed from $m = 1$ to M, for $M = 1$, 5, 10, 20, and 60 repetitions. Constant background counts are subtracted. (**D**) Amplitudes $|A_m|$ for Rabi oscillation measurements obtained from the mth readout normalized to the signal amplitude without repetitive readout (A_0). (**E**) Improvement in SNR using the repetitive readout scheme. Blue curves in (D) and (E) are simulations with imperfection parameters estimated from independent experiments (*25*).

was considered. The state of spin **e** may be correlated with a more distant spin $\mathbf{n}_2$ in addition to proximal spin $\mathbf{n}_1$. As the decay time of spin $\mathbf{n}_2$ is longer than that of spin $\mathbf{n}_1$ because of a weaker interaction with spin **e**, the information stored in spin $\mathbf{n}_2$ persists after spin $\mathbf{n}_1$ has been depolarized under optical illumination. This remaining $\mathbf{n}_2$ polarization can then be transferred to spin $\mathbf{n}_1$ and repetitively readout again.

Control of two nuclear spins is achieved by using the strongly coupled nuclear spin $\mathbf{n}_1$ as a probe for the second nearby ^{13}C nuclear spin $\mathbf{n}_2$, which cannot be directly observed via the NV center. By placing the NV electronic spin in $|0\rangle_e$ state, the hyperfine coupling is removed. This enables proximal ^{13}C nuclear spins with similar Zeeman energy to flip-flop and exchange spin population. Figure 3D shows that the nuclear population, $p_{n1,\uparrow}(\tau)$, oscillates between $p_{n1,\uparrow}(0) \approx 0.2$ and $p_{n1,\uparrow}(T/2) \approx 0.5$ with a period of $T = 117$ (1) μs (Fig. 3, A and C). The relatively high contrast of these oscillations suggests an interaction with a second nuclear spin ($\mathbf{n}_2$) as the two nuclei flip-flop between the states $|\uparrow\rangle_{n1}|\downarrow\rangle_{n2}$ and $|\downarrow\rangle_{n1}|\uparrow\rangle_{n2}$. Such an excitation exchange requires a similar Zeeman splitting for the two spins, indicating that the second nucleus is also a ^{13}C. The nuclear spin-spin interaction strength determined by our measurements, $b = \pi/T = 4.27$ (3) kHz, is several times that of a bare dipolar coupling (2 kHz for two ^{13}C nuclei separated by the nearest neighbor distance, 1.54 Å), signifying that their interaction is mediated by the NV electronic spin (Fig. 3A, inset) (*25*), which is described by the interaction hamiltonian $H_{\text{int}} = b(I_{1+}I_{2-} + I_{1-}I_{2+})$. This interaction can be used to effectively control the state of the second nucleus and of the entire three-spin system. Specifically, a half period of nuclear spin oscillation, $T/2$, constitutes a SWAP (*1*) operation between the two nuclear spins. This operation can be used, for example, to polarize the second nuclear spin (Fig. 3, C and D). In addition, by modifying the initial state of spin $\mathbf{n}_1$, we can prepare the initial state of the two nuclei in any of the four possible configurations: ↑↑, ↑↓, ↓↑, or ↓↓ (*25*). Further control is provided by putting the electronic spin into the $|1\rangle_e$ state, in which case the flip-flop dynamics between spins $\mathbf{n}_1$ and $\mathbf{n}_2$ disappears (fig. S1). This is because spins $\mathbf{n}_1$ and $\mathbf{n}_2$ typically have very distinct hyperfine splittings that introduce a large energy difference ($\Delta E >> b$) between $|\uparrow\rangle_{n1}|\downarrow\rangle_{n2}$ and $|\downarrow\rangle_{n1}|\uparrow\rangle_{n2}$ and quench the interaction. Therefore, we can implement a controlled-SWAP operation between spins $\mathbf{n}_1$ and $\mathbf{n}_2$, enabling full control over spin $\mathbf{n}_2$. We further observed that spin $\mathbf{n}_2$ has a decay time of $\tau_{n2} = 53$ (1) μs (Fig. 3B, inset) under

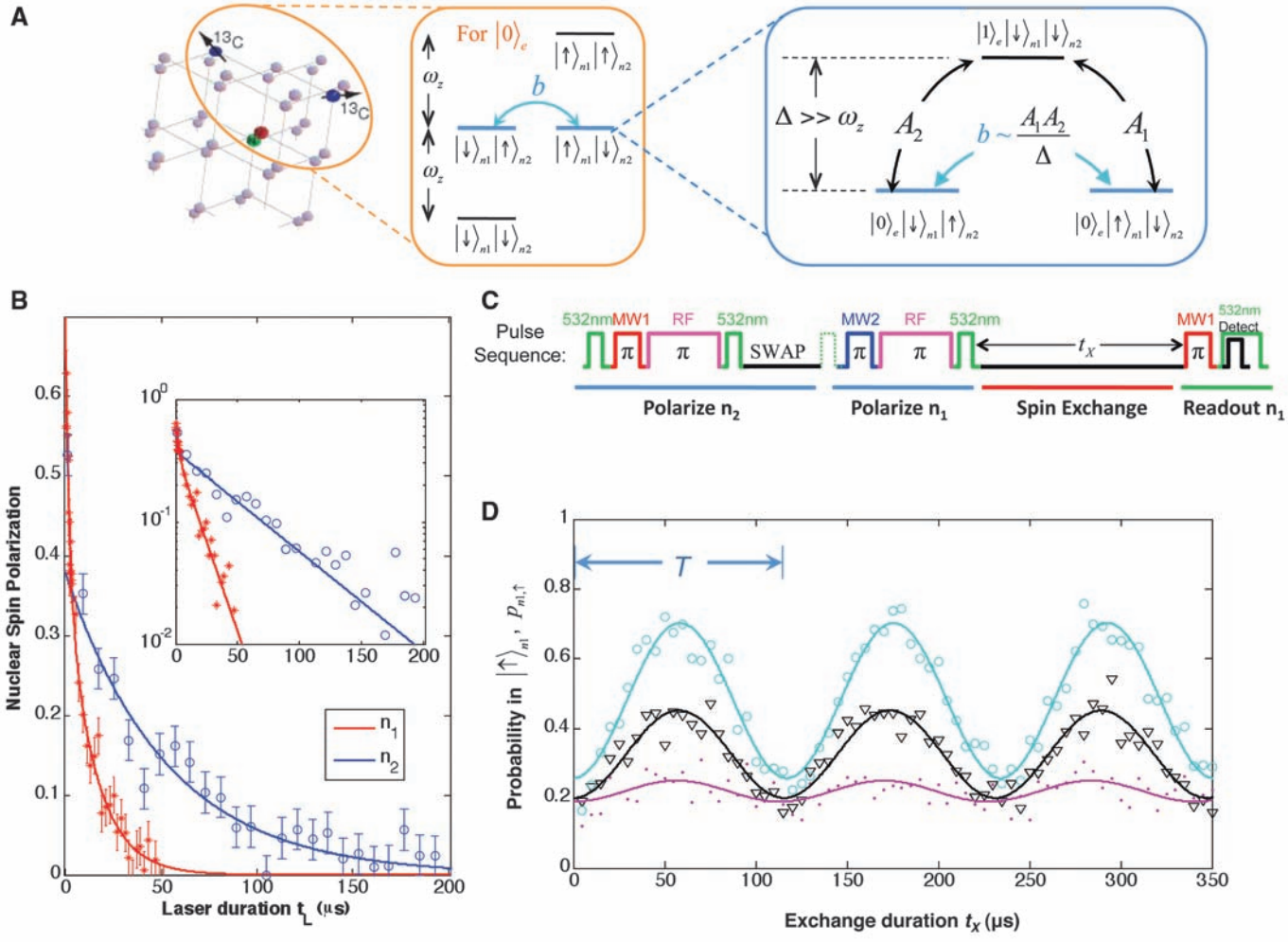

Fig. 3. Coherence and control of two nuclear spins. (**A**) The coupled spin system formed by the NV electronic spin (**e**) and two proximal ^{13}C nuclear spins ($\mathbf{n}_1$ and $\mathbf{n}_2$). (Middle) Energy levels for spins $\mathbf{n}_1$ and $\mathbf{n}_2$ when spin **e** is in the $|0\rangle_e$ state. (Right) Schematic of flip-flop between spins $\mathbf{n}_1$ and $\mathbf{n}_2$, which is electron-mediated by the second-order hopping via $|1\rangle_e|\downarrow\rangle_{n1}|\downarrow\rangle_{n2}$. (**B**) Measured depolarization of spins $\mathbf{n}_1$ and $\mathbf{n}_2$ under optical illumination. For the duration of optical illumination t_L longer than 1 μs, the polarizations for spins $\mathbf{n}_1$ and $\mathbf{n}_2$ decay exponentially with characteristic times $\tau_{n1} = 13$ (1) μs and $\tau_{n2} = 53$ (5) μs, respectively. For t_L less than 1 μs, the decay is slightly faster, which is probably associated with dynamics of the spin-fluctuator model that describe optically induced depolarization of single nuclei (*22*, *25*). These decay times are much longer than the optical readout/pump time of the electronic spin (about 350 ns). (Inset) Log-linear plot. (**C**) Operations and pulse sequence to probe dynamics between spins $\mathbf{n}_1$ and $\mathbf{n}_2$. (**D**) Measured spin flip-flop dynamics between spins $\mathbf{n}_1$ and $\mathbf{n}_2$. For three different preparations of the initial state [$|\downarrow\rangle_{n1}|\uparrow\rangle_{n2}$ (blue), $|\downarrow\rangle_{n1}$ and n_2 in thermal state (black), and $|\downarrow\rangle_{n1}|\downarrow\rangle_{n2}$ (purple)], the observed population, $p_{n1,\uparrow}(t)$, oscillates with the same period $T = 117$ (1) μs. These observations verify the theoretical prediction, with flip-flop coupling strength $b = 4.27$ (3) kHz.

optical illumination. Compared with spin $\mathbf{n}_1$, spin $\mathbf{n}_2$ is less perturbed by the optical transitions between different electronic states because it has a weaker hyperfine coupling to the electron (*22*).

To demonstrate concatenated readout experimentally, both nuclear spins were initialized in the state $|\downarrow\rangle_{n1}\,|\downarrow\rangle_{n2}$, and a single NV electronic spin that we would like to detect was prepared in a superposition state $(\alpha|0\rangle + \beta|1\rangle)_e$. First, the operation ($C_eNOT_{n1}$-SWAP-$C_eNOT_{n1}$) was used to prepare the GHZ-type state $|\Psi\rangle = \alpha|0\rangle_e\,|\downarrow\rangle_{n1}\,|\downarrow\rangle_{n2} + \beta|1\rangle_e\,|\uparrow\rangle_{n1}\,|\uparrow\rangle_{n2}$. Next, we optically readout/pumped spin **e**, leaving the system in state $\rho'_{post} = |\alpha|^2\,|0\downarrow\downarrow\rangle\langle 0\downarrow\downarrow| + |\beta|^2\,|0\uparrow\uparrow\rangle\langle 0\uparrow\uparrow|$. $M-1$ repetitive readouts of spin $\mathbf{n}_1$ were then performed in the manner described above until spin $\mathbf{n}_1$ was depolarized. At that point, spin $\mathbf{n}_2$ was still directly correlated with the first measurement of the **e** spin. This information can be transferred to spin $\mathbf{n}_1$ by means of a nuclear SWAP gate. Thus, the parity information can be measured again by performing a second round of M-step repetitive readout. These operations are summarized in the quantum circuit (Fig. 4A) and pulse sequences (Fig. 4B).

Experimentally, the "revival" in the signal amplitude $|A_m|$ after the SWAP was demonstrated (Fig. 4C), which led to an associated jump in the SNR curve (Fig. 4D) for $M' = 61$. This shows that the second nuclear spin can be used to further enhance the readout efficiency. Although ideally the repetitive readout scheme assisted by two nuclear spins should improve the absolute SNR more than a single nuclear spin, in the present experimental realization this is not yet so because more errors are accumulated for the two-nuclear-spin scheme because of initialization and pulse imperfections. These errors reduce the optical signal amplitudes for the readout assisted by two nuclear spins, compromising the overall SNR improvement. Nevertheless, the experiments clearly demonstrate that it is in principle possible to further boost the relative SNR by using additional nuclear spins.

Although we have demonstrated an enhancement for coherent Rabi oscillations, any set of pulses acting on the electronic spin (such as a spin echo sequence) can be implemented. This should have immediate applications to NV-based nanomagnetometry (*26*, *27*). Because the duration of the entire repetitive readout sequence (~150 μs in Fig. 2B) is shorter than the typical echo duration in pure diamond, SNR improvements directly translate into enhanced sensitivity and increased speed of nanoscale diamond magnetometer (*28*). This may have important applications in probing time-varying processes in biophysical systems. The repetitive readout can also be used to achieve single-shot readout of NV centers. At room temperature, with optimized collection efficiency, an improvement in spin signal on the order of a few hundred is needed to achieve single-shot readout. Potentially, this improvement can be obtained by using nuclei more robust to optical depolarization, such as the nitrogen nuclear spin of the NV center in isotopically pure ^{12}C diamond (*19*) and by using advanced control techniques (*29*, *30*) to suppress the imperfections from microwave pulses. Furthermore, resonant optical excitations [wavelength $\lambda \approx 637$ nm] can be used for NV centers at cryogenic temperatures. Here, the resolved spin structure of optical excited states (*20*, *31*, *32*) can be exploited to readout the electronic spin much more efficiently with reduced perturbation to the nuclear spin (*22*). Under these conditions, a 10-fold spin signal improvement may be sufficient to enable single-shot readout of the NV electronic spin. In turn, this can be used to perform robust, adaptive QND measurements of nuclear-spin qubits, which will be of direct use for distributed quantum networks (*13*, *21*). Our experiments demonstrate that manipulation of several nuclear-spin ancillae surrounding a central electronic spin can be used to implement useful quantum algorithms in solid-state systems.

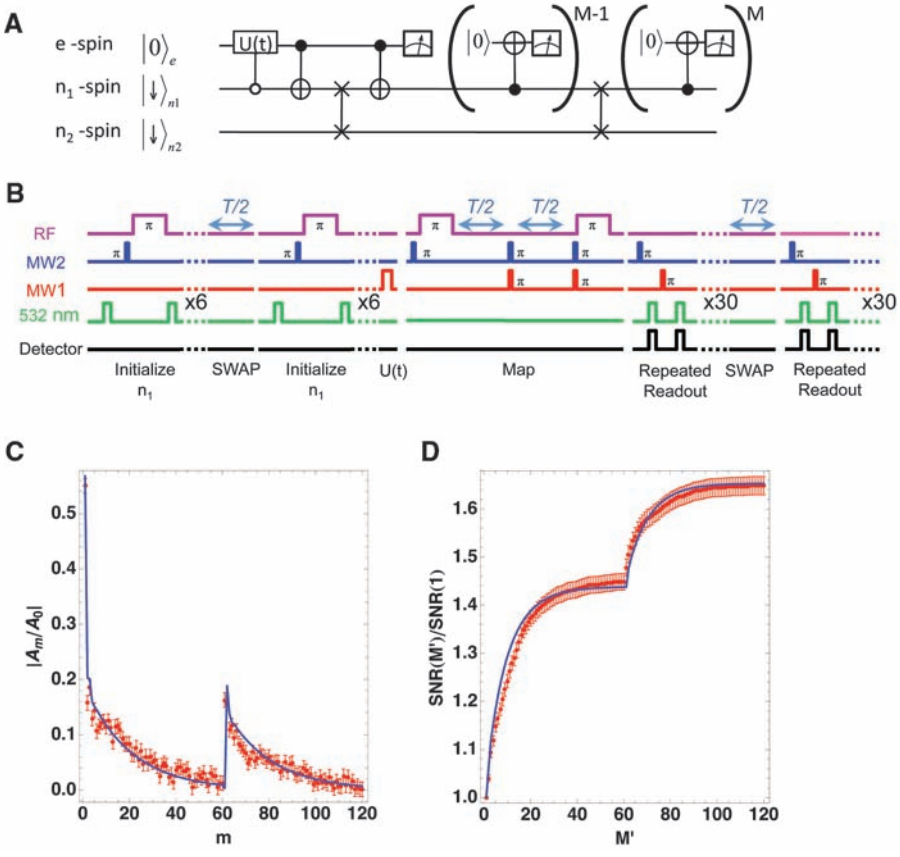

Fig. 4. Demonstration of the two-level concatenated readout procedure. (**A**) Quantum circuit for concatenated M-step repetitive readout scheme assisted by both spins $\mathbf{n}_1$ and $\mathbf{n}_2$. (**B**) Operations and pulse sequences for $M = 60$. Ideally, the GHZ-like state $\alpha|0\rangle_e\,|\downarrow\rangle_{n1}\,|\downarrow\rangle_{n2} + \beta|1\rangle_e\,|\uparrow\rangle_{n1}\,|\uparrow\rangle_{n2}$ with the parity information of spin **e** imprinted on both spins $\mathbf{n}_1$ and $\mathbf{n}_2$ is created before the first readout. After the first round of M-step repetitive readout, spin $\mathbf{n}_1$ is depolarized, but spin $\mathbf{n}_2$ maintains its polarization. The spin state of spin $\mathbf{n}_2$ is swapped to spin $\mathbf{n}_1$, which is then detected during the second round of M-step repetitive readouts. (**C**) Normalized amplitude $|A_m|/|A_0|$ obtained from the mth readout. (**D**) Measured improvement in the SNR by use of the double repetitive readout scheme. The blue curves in (C) and (D) are simulations with imperfection parameters estimated from independent experiments (*25*).

References and Notes

1. R. Blatt, D. Wineland, *Nature* **453**, 1008 (2008).
2. R. Hanson, D. D. Awschalom, *Nature* **453**, 1043 (2008).
3. M. Riebe *et al.*, *Nature* **429**, 734 (2004).
4. R. Reichle *et al.*, *Nature* **443**, 838 (2006).
5. L. DiCarlo *et al.*, *Nature* **460**, 240 (2009).
6. C. A. Ryan, C. Negrevergne, M. Laforest, E. Knill, R. Laflamme, *Phys. Rev. A* **78**, 012328 (2008).
7. T. Rosenband *et al.*, *Science* **319**, 1808 (2008).
8. D. B. Hume, T. Rosenband, D. J. Wineland, *Phys. Rev. Lett.* **99**, 120502 (2007).
9. W. M. Witzel, S. Das Sarma, *Phys. Rev. B* **77**, 165319 (2008).
10. J. Maze, J. M. Taylor, M. D. Lukin, *Phys. Rev. B* **78**, 094303 (2008).
11. W. A. Coish, J. Fischer, D. Loss, *Phys. Rev. B* **77**, 125329 (2008).
12. F. Jelezko *et al.*, *Phys. Rev. Lett.* **93**, 130501 (2004).
13. M. V. G. Dutt *et al.*, *Science* **316**, 1312 (2007).
14. P. Neumann *et al.*, *Science* **320**, 1326 (2008).
15. R. Hanson, V. V. Dobrovitski, A. E. Feiguin, O. Gywat, D. D. Awschalom, *Science* **320**, 352 (2008).
16. J. J. L. Morton *et al.*, *Nat. Phys.* **2**, 40 (2006).
17. J. S. Hodges, J. C. Yang, C. Ramanathan, D. G. Cory, *Phys. Rev. A* **78**, 010303 (2008).
18. J. J. L. Morton *et al.*, *Nature* **455**, 1085 (2008).
19. G. Balasubramanian *et al.*, *Nat. Mater.* **8**, 383 (2009).
20. G. D. Fuchs *et al.*, *Phys. Rev. Lett.* **101**, 117601 (2008).
21. L. Jiang, J. M. Taylor, A. S. Sorensen, M. D. Lukin, *Phys. Rev. A* **76**, 062323 (2007).
22. L. Jiang *et al.*, *Phys. Rev. Lett.* **100**, 073001 (2008).
23. S. Haroche, J. M. Raimond, *Exploring the Quantum: Atoms, Cavities, and Photons* (Oxford Univ. Press, New York, 2006).
24. M. Sarovar, K. C. Young, T. Schenkel, K. B. Whaley, *Phys. Rev. B* **78**, 245302 (2008).
25. Materials and methods are available as supporting material on *Science* Online.

26. J. R. Maze *et al.*, *Nature* **455**, 644 (2008).
27. G. Balasubramanian *et al.*, *Nature* **455**, 648 (2008).
28. J. M. Taylor *et al.*, *Nat. Phys.* **4**, 810 (2008).
29. N. Khaneja, T. Reiss, C. Kehlet, T. Schulte-Herbruggen, S. J. Glaser, *J. Magn. Reson.* **172**, 296 (2005).
30. P. Cappellaro, L. Jiang, J. S. Hodges, M. D. Lukin, *Phys. Rev. Lett.* **102**, 210502 (2009).
31. N. B. Manson, J. P. Harrison, M. J. Sellars, *Phys. Rev. B* **74**, 104303 (2006).
32. A. Batalov *et al.*, *Phys. Rev. Lett.* **102**, 195506 (2009).

33. We thank P. Cappellaro, L. Childress, J. Doyle, M. V. G. Dutt, J. MacArthur, A. Sorenson, P. Stanwix, E. Togan, and A. Trifonov for many stimulating discussions and experimental help. This work was supported by the Defense Advanced Research Projects Agency, NSF, the Packard Foundation, and the Pappalardo Fellowship. The content of the information does not necessarily reflect the position or the policy of the U.S. Government, and no official endorsement should be inferred.

Supporting Online Material
www.sciencemag.org/cgi/content/full/1176496/DC1
Materials and Methods
Figs. S1 to S4
References

19 May 2009; accepted 29 July 2009
Published online 10 September 2009;
10.1126/science.1176496
Include this information when citing this paper.

Persistent Currents in Normal Metal Rings

A. C. Bleszynski-Jayich,[1] W. E. Shanks,[1] B. Peaudecerf,[1] E. Ginossar,[1] F. von Oppen,[2] L. Glazman,[1,3] J. G. E. Harris[1,3]

Quantum mechanics predicts that the equilibrium state of a resistive metal ring will contain a dissipationless current. This persistent current has been the focus of considerable theoretical and experimental work, but its basic properties remain a topic of controversy. The main experimental challenges in studying persistent currents have been the small signals they produce and their exceptional sensitivity to their environment. We have developed a technique for detecting persistent currents that allows us to measure the persistent current in metal rings over a wide range of temperatures, ring sizes, and magnetic fields. Measurements of both a single ring and arrays of rings agree well with calculations based on a model of non-interacting electrons.

An electrical current induced in a resistive circuit will rapidly decay in the absence of an applied voltage. This decay reflects the tendency of the circuit's electrons to dissipate energy and relax to their ground state. However, quantum mechanics predicts that the electrons' many-body ground state (and, at finite temperature, their thermal equilibrium state) may contain a persistent current (PC), which flows through the resistive circuit without dissipating energy or decaying. A dissipationless equilibrium current flowing through a resistive circuit is counterintuitive, but it has a familiar analog in atomic physics: Some atomic species' electronic ground states possess nonzero orbital angular momentum, which is equivalent to a current circulating around the atom.

One of the major insights of mesoscopic condensed-matter physics is that this analogy remains valid even when the electrons experience a static disorder potential, as in a resistive metal (*1*). Theoretical treatments of PCs in resistive metal rings have been developed over a number of decades [see (*1*, *2*) and references therein]. Calculations that take into account the electrons' inevitable coupling to the static disorder potential and a fluctuating thermal bath predict several general features. A micrometer-diameter ring will support a PC of $I \sim 1$ nA at temperatures $T \lesssim 1$ K. A magnetic flux Φ threading the ring will break time-reversal symmetry, allowing the PC to flow in a particular direction around the ring. Furthermore, the Aharonov-Bohm effect will require I to be periodic in Φ with period $\Phi_0 = h/e$, thereby providing a clear-cut experimental signature of the PC.

These predictions have attracted considerable interest, but measuring the PC is challenging for a number of reasons. For example, the PC flows only within the ring and so cannot be measured with a conventional ammeter. Experiments to date (*2*, *3*) have mostly used superconducting quantum interference devices (SQUIDs) to infer the PC from the magnetic field it produces. Interpretation of these measurements has been complicated by the SQUID's low signal-to-noise ratio (SNR) and the uncontrolled back action of the SQUID's ac Josephson oscillations, which may drive nonequilibrium currents in the rings. In addition, SQUIDs perform optimally in low magnetic fields; this limits the maximum Φ that can be applied to the rings, allowing observation of only a few oscillations of $I(\Phi)$ and complicating the subtraction of background signals unrelated to the PC.

Experiments to date have produced a number of confusing results in apparent contradiction with theory and even among the experiments themselves (*2*, *3*). These conflicts have remained without a clear resolution for nearly 20 years, suggesting that our understanding of how to measure and/or calculate the ground-state properties of as simple a system as an isolated metal ring may be incomplete.

More recent theoretical work has predicted that the PC is highly sensitive to a variety of subtle effects, including electron-electron interactions (*4*–*7*), the ring's coupling to its electromagnetic environment (*8*), and trace magnetic impurities within the ring (*9*). These theories have not explained all of the experimental results to date, but they do indicate that accurate measurements of the PC would be able to address a number of interesting questions in many-body condensed-matter physics (in addition to resolving the long-standing controversy described above).

We measured the PC in resistive metal rings using a micromechanical detector with orders of magnitude greater sensitivity and lower back-action than SQUID-based detectors. Our approach allows us to measure the PC in a single ring and arrays of rings as a function of ring size, temperature, and the magnitude and orientation of the magnetic field over a much broader range than has been possible previously. Quantitative agreement is found between these measurements and calculations based on a model of diffusive, non-interacting electrons. This agreement is supported by independent measurements of the rings' electrical properties.

Figure 1, A to C, shows single-crystal Si cantilevers with integrated Al rings [their fabrication is described elsewhere (*10*)]. All the PC measurements were made in magnetic fields well above the critical field of Al, ensuring that the rings were in their normal (rather than superconducting) state. The parameters of the four ring samples measured are given in Table 1.

In the presence of a magnetic field $\vec{B}$, each ring's current I produces a torque on the cantilever $\vec{\tau} = \vec{\mu} \times \vec{B}$ as well as a shift $\delta\nu$ in the cantilever's resonant frequency ν. Here $\vec{\mu} = \pi r^2 I \hat{n}$ is the magnetic moment of the PC, r is the ring radius, and $\hat{n}$ is the unit vector normal to the ring. We infer $I(B)$ from measurements of $\delta\nu(B)$; the conversion between $\delta\nu(B)$ and $I(B)$ is described in the supporting online material (SOM) text.

To monitor ν, we drive the cantilever in a phase-locked loop. The cantilever is driven via a piezoelectric element, and the cantilever's displacement is monitored by a fiber-optic interferometer (*11*). The cantilever's thermally limited force sensitivity is ~2.9 aN/Hz$^{1/2}$ at T = 300 mK, corresponding to a magnetic moment sensitivity of ~11 μ_B/Hz$^{1/2}$ and a current sensitivity of ~20 pA/Hz$^{1/2}$ for a ring with r = 400 nm at B = 8 T. By comparison, SQUID magnetometers achieve a current sensitivity $\gtrsim$5 nA/Hz$^{1/2}$ for a similar ring (*12*–*14*). The noise temperature of the cantilever and the electron temperature of a metal sample at the end of a cantilever both equilibrate with the fridge temperature for the conditions we used (*11*).

The frequency shift of a cantilever containing an array of N = 1680 lithographically identical rings with r = 308 nm at T = 323 mK is shown (Fig. 1D) as a function of B. Oscillations with a period $\approx$20 mT, corresponding to a flux h/e through each ring, are visible in the raw data. Depending on r and θ (the angle between $\vec{B}$ and the plane of

[1]Department of Physics, Yale University, New Haven, CT 06520, USA. [2]Institut für Theoretische Physik, Freie Universität Berlin, Fachbereich Physik, 14195 Berlin, Germany. [3]Department of Applied Physics, Yale University, New Haven, CT 06520, USA.

Supporting Online Material for

Repetitive readout of a single electronic spin via quantum logic with nuclear spin ancillae

L. Jiang, J. S. Hodges, J. R. Maze, P. Maurer, J. M. Taylor, D. G. Cory, P. R. Hemmer, R. L. Walsworth, A. Yacoby, A. S. Zibrov, M. D. Lukin

S.1. EXPERIMENTAL METHODS

S.1.1. Experimental setup

We isolate single NV centers using standard confocal microscopy techniques. The NV centers are optically excited using green light (λ_{ex} = 532 nm, sourced from a Coherent Compass 315M-100 laser). We focus the green spot to a nearly diffraction-limited spot-size using an oil immersion objective (Nikon CFI Apochromat TIRF 100X, NA = 1.49) focused to a depth of up to 50 μm below the diamond surface. Fluorescence emission from the lowest lying excited triplet state (^3E level of NV [*S1*]) is collected within the phonon sideband, extending from 650 nm to 750 nm. This light is focused onto a single-mode optical fiber (NA=.12, MFD = 4.3μm), which acts as a small aperture spatial filter and rejects light emanating from outside the focal plane. Photons incident on the fiber are detected using an avalanche photodiode module (PerkinElmer SPCM-AQR-13).

In order to find a single NV center within the diamond, we image a 50μm x 50μm area within a fixed focal plane by changing the incidence angle of the excitation light wavefronts at the objective. This is accomplished by using a fast, closed-loop XY scanning mirror system (Cambridge Technology, 6215H scanning mirrors). Different focal planes are examined by moving the entire sample, along the tube axis of the objective, using a closed-loop z-axis piezo stage (Physique Instrument, P-620.ZCD). The density of NV centers within the sample is small enough that we can resolve single bright spots and collect light from these emitters. In order to verify that these spots are single centers, we measure the autocorrelation function of the emitted light in a Hanbury-Brown-Twiss style setup ($g^{(2)}(\tau)$). Furthermore, we monitor

the fluorescence intensity under resonant microwave excitation to verify that these single emitters are indeed nitrogen-vacancy centers, with a finite ESR response near 2.87 GHz at zero applied magnetic field. If an NV center is strongly coupled to a ^{13}C spin within the lattice, this appears as an additional splitting in the the spectrum of microwave response.

The nitrogen-vacancy color centers used for our repetitive readout experiments are found within a bulk, single crystal type IIa natural diamond with a remarkably low native nitrogen impurity concentration. The lack of paramagnetic defects in this sample is believed to be the primary reason for long ($> 500\mu s$) spin dephasing times of the NV center electronic spin. The ^{13}C nuclei within the lattice are randomly distributed and have a natural isotope fraction, 1.1% relative to all carbon nuclei.

S.1.2. Spin Control of the NV centers

At room temperature, the three spin eigenstates of the NV center ($|0\rangle_e$, $|1\rangle_e$, and $|-1\rangle_e$) are equally populated. Optical excitation at 532 nm, excites the ground state triplet of the NV to an excited vibronic state, which decays to the first excited triplet state. The population in these spin states will either radiatively decay back to the ground state or undergo an intersystem crossover to a metastable singlet state, which decays into the $|0\rangle_e$ state. This provides a mechanism for optical pumping of the NV center spin. After 1 μs period of illumination (near optical saturation) the $|\pm 1\rangle_e$ states are optically pumped to the $|0\rangle_e$ state in excess of 95%. This conveniently prepares an initial state $|0\rangle_e$ after readout, but barely perturbs the nuclear spin state.

We apply microwave and radiofrequency (RF) fields to individual NV centers by driving a small copper wire (15μm diameter) placed on the diamond surface and secured to a 50Ω impedance matched microstrip transmission line. Three separate frequency synthesizers are used to generate the three frequencies needed for obtain full spin control of the electronic-nuclear spin system, identified as MW1, MW2 and RF in Figure 1D of the main text. These values are cited below. Separate amplifiers for the microwave (OphirRF, S-Band, 15W, Model XRF738) and RF (ENI, 10W, Model 310-L) allow us to generate magnetic fields of about 10 gauss. Short microwave pulses, on the order of 10ns, are generated by gating an SPST switch with an extremely short rise time (Custom Microwave Components S0947A-02, rise time 3ns). Timing of the counter gating, RF and microwave pulses and the

acousto-optic modulator (AOM) is coordinated by a multiple channel TTL pulse generator (SpinCore PulseBlaster ESR-Pro, 400MHz), with up to 2.5ns timing resolution.

For pulsed experiments, measurement of the spin state involves counting the NV fluorescent photons after optical pumping. This involves monitoring the phonon side band fluorescence under optical excitation within 100-500ns [*S1*]. Short optical pulses are achieved using an AOM with a digital driver (Isomet 1250C-848) in a double-pass setup [*S2*]. Rise times of the optical pulses are about 20ns and thus enable sufficient contrast between the two spin states.

In order to remove systematic fluctuations in the counting rates of the fluorescent photons (e.g., heating and defocusing of the NV due to long microwave pulses), we take a series of measurements before *each* run of the experiment. Prior to any of our repeated readout experiments, we measure the fluorescence after the following microwave pulse configurations: (1) no microwave pulse, (2) a single MW1 π-pulse, (3) a single MW2 π-pulse, and (4) a MW1 and MW2 π-pulse. Conditions (1) and (4) set the maximum and minimum count rates for the NV center readout and set the relative scale for the Rabi experiments (Figure 1 of main text).

Random, slow drifting of the counting rates of the NV center (e.g., due to day/night temperature cycles or mechanical perturbations) are accounted for by a software-based feedback mechanism. Prior to each experimental average ($\sim 10^5$ repetitions), we take a reference count rate of the NV fluorescence. If this is outside an allowed threshold, we vary the scanning mirror and piezo stage voltages in order to maximize the counting rate. In this way, defocusing of the NV center can be corrected and stabilized. Over the course of six months, such tracking has enabled us to study the same center exclusively.

S.1.3. Magnetic field, microwave and RF control pulses

We use three sets of orthogonal coil windings in a quasi-Helmholtz configuration to apply the static magnetic field for tuning the spin resonance of the NV. Each winding consists of roughly 100 turns and each pair can generate up to 40 gauss in three orthogonal directions when driven with 4A, direct current. By independently changing the current supplied to each coil pair, we can align the magnetic field vector relative to the axis of symmetry of the NV center ($\hat{z}$). Coarse measurements of the magnetic field amplitudes are made using

a three-axis Hall sensor (Ametes MFS-3A). For more precise alignment, we measure the ESR response of the NV in both a continuous wave and pulsed (electron spin echo envelope modulation) manner, as described below.

As shown in Fig. 1A, we use MW1 to drive the transition between $|0\rangle_e|\downarrow\rangle_{n1}$ and $|1\rangle_e|\downarrow\rangle_{n1}$, and MW2 for the transition between $|0\rangle_e|\uparrow\rangle_{n1}$ and $|1\rangle_e|\uparrow\rangle_{n1}$. The two transitions differ in energy by $\delta = (2\pi)\times 13.675\,(1)$ MHz, mostly due to the hyperfine interaction between spins $\mathbf{e}$ and $\mathbf{n}_1$. When the microwave (MW) Rabi frequency Ω_{MW} is comparable to the detuning δ, the effect of off-resonant driving should be considered. For example, when trying to drive microwave transitions for only levels with the nuclear spin in $|\downarrow\rangle_{n1}$, we may also change the populations for the $|\uparrow\rangle_{n1}$ levels. Fortunately, if we are only interested in π-pulses, the effect of off-resonant driving can be suppressed. We choose the bare MW Rabi frequency $\Omega_{MW} = \delta/\sqrt{3} = (2\pi)\times 7.89$ MHz with pulse duration π/Ω_{MW}, which performs a π rotation for the resonant transition. For the δ-detuned transition, the effective Rabi frequency is $\sqrt{\Omega_{MW}^2+\delta^2} = \sqrt{\Omega_{MW}^2+3\Omega_{MW}^2} = 2\Omega_{MW}$, and the operation gives a (trivial) 2π rotation. Thus, in principle, we can achieve a perfect $\mathrm{C}_{n1}\mathrm{NOT}_e$ gate with an MW1 (or MW2) π pulse, despite the finite detuning δ.

For our experiment the two microwave resonance frequencies are $\nu_{MW1} = 2.962$ GHz and $\nu_{MW2} = 2.949$ GHz. The radiofrequency field is tuned to the nuclear spin splitting at $\nu_{RF} = 13.675$ MHz. We note that the duration for a π-pulse at this frequency is about 5μs, which indicates a Rabi frequency of almost 100 kHz. This nuclear Rabi frequency is enhanced from that of a bare ^{13}C nucleus ($\gamma_C = 1.1$kHz/ Gauss) due to the pseudo-nuclear Zeeman effect [*S3*]. This effect enhances transitions of the nuclear spin because of the strong hyperfine coupling between the nucleus and the NV electronic spin.

In addition, we must also consider the presence of a ^{14}N nuclear spin, with $I = 1$ and hyperfine coupling strength $\alpha_N = (2\pi)\times 2.1\,(1)$ MHz, which gives the triplet splitting for both transition lines in the ESR spectrum (Fig. S1). At room temperature, the ^{14}N nuclear spin is unpolarized (i.e., in a completely mixed state), with equal probability in the spin states $I_z = 0, \pm 1$.

The splitting associated with ^{14}N nuclear spin can introduce a small detuning $\pm\alpha_N$ to the resonant transition, resulting in an error probability $\sim (\alpha_N/\Omega_{MW})^2$. We estimate the average error probability for the MW π-pulse to be $\varepsilon_{\mathrm{res}}^{MW} \approx 0.07$ for the resonant transition. In addition, the splitting associated with ^{14}N can also affect the δ-detuned transition. In the

presence of extra detuning $\pm\alpha_N$, the 2π rotation for the δ-detuned transition is no longer perfect. The estimated average error probability for the MW π-pulse is $\varepsilon_{\rm det}^{MW} \approx 0.01$ for the δ-detuned transition.

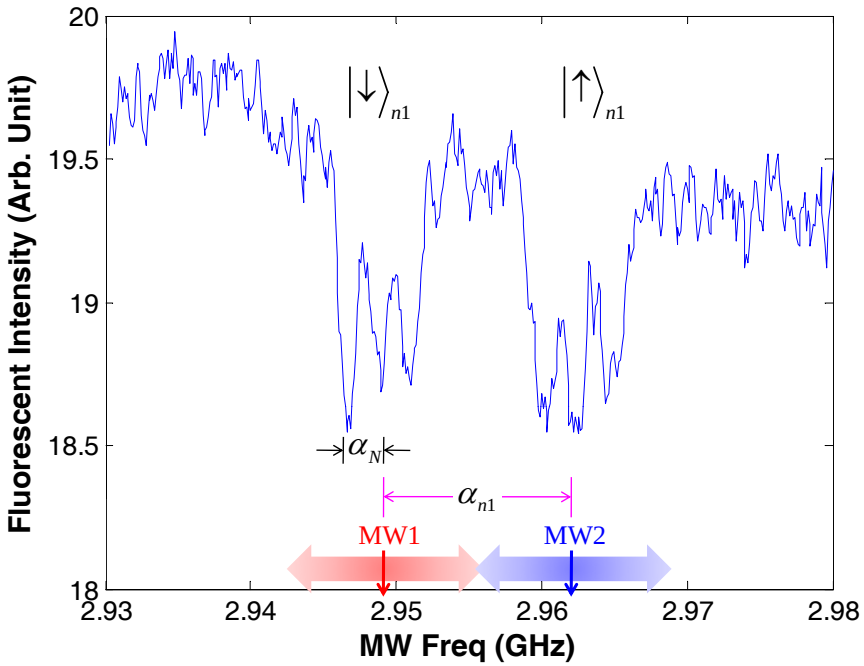

Figure S1: Fluorescence detected electron spin resonance of the NV center. We monitor the fluorescence under optical excitation at λ_{ex} while sweeping the carrier microwave frequency. When the resonance condition is met, we see a drop in the count rate, signifying a transfer of population to the $m_s = \pm 1$ states. Here we show only the portion of the spectrum involving transitions between $m_s = 0$ and 1. In the absence of any nuclear spins, this condition would occur at single frequency, but is split due to the hyperfine interaction with nearby nuclear spins. The six lines shown correspond to coupling of the NV to a nearby ^{13}C ($\mathbf{n_1}, I = 1/2$) and ^{14}N ($I = 1$) with hyperfine couplings α_N and α_{n1} respectively. The two microwave driving frequencies (MW1 and MW2) address the $|\downarrow\rangle_{n1}$ and $|\uparrow\rangle_{n1}$ manifolds and differ in frequency by α_{n1}. The MW Rabi frequency ($\Omega = 7.89$ MHz) is sufficiently large to drive the triplet lineshape for each manifold.

S.2. EFFECTIVE HAMILTONIAN

In this section, we start with the full spin Hamiltonian that includes both the electronic spin and the nuclear spins. We obtain the effective Hamiltonian using time-independent perturbation theory. We then study the hyperfine coupling associated with the first nuclear spin ($\mathbf{n}_1$) to justify the claim that the quantization axis of spin $\mathbf{n}_1$ is effectively the same when spin $\mathbf{e}$ is $|m_s = 0\rangle_e$ or $|m_s = 1\rangle_e$. Finally, we use the effective Hamiltonian to study the electron-mediated coupling between the two nuclear spins $\mathbf{n}_1$ and $\mathbf{n}_2$.

S.2.1. Full Hamiltonian

To calculate the interaction between nuclear spins, we start with the full spin Hamiltonian for the ground state triplet ($S = 1$) of the NV center electronic spin. We choose a coordinate system with $\hat{z}$ along the NV axis (the [111] crystal axis), $\hat{x}$ and $\hat{y}$ fixed arbitrarily by taking $\hat{x}$ to lie in a horizontal plane with respect to the laboratory coordinates.

First, we start by identifying the physical interactions between the spins of the system, ordered by their energy (descending):

$$H = H_{ZFS} + H_{EZ} + H_{HF} + H_{NQ} + H_{NZ} + H_{DD}. \tag{S1}$$

H_{ZFS} is the zero field splitting term, due to the spin-spin interaction of the two unpaired electrons comprising the NV center [*S1*]. H_{EZ} is the Zeeman interaction between the electron and an applied magnetic field B. H_{HF} is the hyperfine interaction between the electronic spin and any nuclear spin within the diamond lattice. In general, it will have an isotropic Fermi contact contribution and a dipole-dipole contribution. H_{NQ} is the nuclear quadrupolar splitting for nuclei with spin angular momentum $I \geq 1$. Only the ^{14}N nuclear spin of the NV center ($I = 1$) has a quadrupolar coupling. Since it was shown in [*S4*] that this spin is a constant of the motion, we hereby drop the quadrupolar term from the calculation. H_{NZ} is the nuclear Zeeman interaction between the external magnetic field and a nuclear magnetic moment. Finally, H_{DD} is the dipole-dipole interaction between two nuclear spins.

At static magnetic fields much smaller than 100 mT, the symmetry axis of the zero field splitting ($\hat{z}$) defines the quantization axis for the NV center. In this coordinate system the zero field splitting is:

$$H_{ZFS} = \Delta(S_z^2 - \frac{1}{3}S^2) + E(S_x^2 - S_y^2) \tag{S2}$$

For the ground state of the NV center, $\Delta = (2\pi) \times 2.87$ GHz and $E \approx 0$ for perfect C_{3v} symmetry. We can then decompose the Hamiltonian into secular ($\|$) and non-secular ($\perp$) terms, depending on whether or not parts of the various interactions commute with S_z^2:

$$H = H_{ZFS+EZ,\|} + H_{EZ,\perp} + H_{NZ} + \sum_{\mathsf{j}} \left(H^{\mathsf{j}}_{\mathrm{hf},\|} + H^{\mathsf{j}}_{\mathrm{hf},\perp} \right) + \sum_{\mathsf{j}>\mathsf{k}} H^{\mathsf{j},\mathsf{k}}_{nuc},$$

where the secular ($\|$) and non-secular ($\perp$) terms are:

$$\begin{aligned}
H_{ZFS+EZ,\|} &= \Delta S_z^2 - \gamma_e B_z S_z \\
H_{EZ,\perp} &= -\gamma_e \left(B_x S_x + B_y S_y \right) \\
H_{NZ} &= -\gamma_0 \sum_{\mathsf{j}} \sum_{n=x,y,z} B_n I_n^{(j)} \\
H^{\mathsf{j}}_{\mathrm{HF},\|} &= S_z \sum_{n=x,y,z} \alpha^{\mathsf{j}}_{zn} I^{\mathsf{j}}_n \\
H^{\mathsf{j}}_{\mathrm{HF},\perp} &= \sum_{n=x,y,z} \left(S_x \alpha^{\mathsf{j}}_{xn} + S_y \alpha^{\mathsf{j}}_{yn} \right) I^{\mathsf{j}}_n \\
H^{\mathsf{j},\mathsf{k}}_{DD} &= \sum_{m,n=x,y,z} I^{\mathsf{j}}_m \beta^{\mathsf{j},\mathsf{k}}_{mn} I^{\mathsf{k}}_n,
\end{aligned}$$

Here I^{j} refers to the the j-th nuclear spin, γ_e and γ_0 are the electronic and ^{13}C gyromagnetic ratios, and we note that $\gamma_e < 0$, $\gamma_0 > 0$. (We assume no $\mathbf{g}$ tensor anisotropy for the NV center and have used the convention of $\hbar = 1$.) α^{j}_{mn} is the hyperfine interaction tensor between the electron and the j-th nuclear spin of ^{13}C and $\beta^{\mathsf{j}\mathsf{k}}_{mn}$ are the matrix elements for the dipolar coupling tensor between nuclear spins j and k. (Note that sans-serif superscripts demarcate the spin and are not exponents). For remote nuclear spins, the hyperfine interaction is mostly dipolar in nature, while the Fermi contact interaction dominates for nearby nuclear spins [*S5*].

S.2.2. Deriving the Effective Hamiltonian

Our goal is to calculate the modified interactions of the nuclear spins due to the presence of a strong hyperfine coupling. Since Δ is the largest energy scale, we may write the effective Hamiltonian in a $1/\Delta$ series. The zeroth order terms commute with ΔS_z^2:

$$H_0 = H_{ZFS+EZ,\|} + H_{NZ} + \sum_{\mathsf{j}} H^{\mathsf{j}}_{\mathrm{hf},\|} + \sum_{\mathsf{j}>\mathsf{k}} H^{\mathsf{j},\mathsf{k}}_{nuc}. \tag{S3}$$

The next order correction is due to the virtual transitions between m_s sub-levels driven by either a transverse external magnetic field or by the hyperfine field of a nearby nuclear spin. The total perturbation is

$$U = H_{EZ,\perp} + \sum_{\mathsf{j}} H^{\mathsf{j}}_{\mathrm{hf},\perp}.$$

Within each m_s subspace (with $m_s = 0, \pm 1$), the first order Hamiltonian $P_{m_s} H_0 + H_1^{m_s}$ can be found by using second order perturbation theory [*S6*]:

$$H_1^{m_s} = P_{m_s} U \frac{1}{E_{m_s} - (\mathbb{1} - P_{m_s}) H_0 (\mathbb{1} - P_{m_s})} U P_{m_s},$$

where $\mathbb{1}$ is the identity operator, $P_{m_s} = |m_s\rangle \langle m_s|_e$ is the projection operator to the subspace with electronic spin projection m_s along the $\hat{z}$ axis, and $E_{m_s} = \Delta m_s^2 - \gamma_e B_z m_s$ is the zeroth-order energy of the electronic spin under $H_{ZFS+EZ,\parallel}$. Using this formalism, we obtain the effective Hamiltonian correction for each m_s subspace:

$$H_1^{m_s} = -\gamma_0 \sum_{\mathsf{j}} \sum_{m,n=x,y,z} B_m \delta g^{\mathsf{j}}_{mn} I^{\mathsf{j}}_n + \sum_{\mathsf{j}>\mathsf{k}} \sum_{m,n=x,y,z} I^{\mathsf{j}}_m \delta \beta^{\mathsf{j},\mathsf{k}}_{mn} I^{\mathsf{k}}_n + \cdots \tag{S4}$$

where the correction of the g-tensor is

$$\delta g^{\mathsf{j}}_{mn}(m_s) = \frac{(3|m_s| - 2)}{\Delta} \left(\frac{\gamma_e}{\gamma_0}\right) \begin{pmatrix} \alpha^{\mathsf{j}}_{xx} & \alpha^{\mathsf{j}}_{xy} & \alpha^{\mathsf{j}}_{xz} \\ \alpha^{\mathsf{j}}_{yx} & \alpha^{\mathsf{j}}_{yy} & \alpha^{\mathsf{j}}_{yz} \\ 0 & 0 & 0 \end{pmatrix}, \tag{S5}$$

and the correction of the nuclear spin interaction due to the electron-mediated process is

$$\delta \beta^{\mathsf{j},\mathsf{k}}(m_s) = \frac{(3|m_s| - 2)}{2\Delta} \begin{pmatrix} \alpha^{\mathsf{j}}_{xx} & \alpha^{\mathsf{j}}_{xy} & \alpha^{\mathsf{j}}_{xz} \\ \alpha^{\mathsf{j}}_{yx} & \alpha^{\mathsf{j}}_{yy} & \alpha^{\mathsf{j}}_{yz} \\ 0 & 0 & 0 \end{pmatrix}^T \begin{pmatrix} \alpha^{\mathsf{k}}_{xx} & \alpha^{\mathsf{k}}_{xy} & \alpha^{\mathsf{k}}_{xz} \\ \alpha^{\mathsf{k}}_{yx} & \alpha^{\mathsf{k}}_{yy} & \alpha^{\mathsf{k}}_{yz} \\ 0 & 0 & 0 \end{pmatrix},$$

or equivalently

$$\delta \beta^{\mathsf{j},\mathsf{k}}_{mn}(m_s) = \frac{(3|m_s| - 2)}{2\Delta} \sum_{l=x,y} \alpha^{\mathsf{j}}_{lm} \alpha^{\mathsf{k}}_{ln}. \tag{S6}$$

Note we have made the assumption that $\Delta \gg |\gamma_e B_z|$.

The first term in Eq.(S4) is the pseudo nuclear Zeeman effect, arising from the enhancement of the external magnetic field due to the hyperfine interaction [*S3*]. The enhancement vanishes when we carefully align the external magnetic field along the NV axis (i.e., $\vec{B} = B_z \vec{e}_z$). This is because $\delta g^{\mathsf{j}}_{zn}(m_s) \equiv 0$ (i.e., all elements vanish in the third row of

Eq. (S5)), and consequently there is *no enhancement* for external magnetic field along the $\hat{z}$ (i.e., NV) axis. Thus, all ^{13}C nuclear spins share the *same* quantization axis (i.e., along the NV axis) and they have the *same* Zeeman splitting $\omega_0 = \gamma_0 B_z \approx 32\,(1)$ kHz, regardless of the individual hyperfine interactions [*S13*]. The second term in Eq.(S4) is the electron-mediated interaction among the nuclear spins, with the correction to the dipolar interaction tensor.

Therefore, we obtain the effective Hamiltonian of the nuclear spin for each m_s subspace

$$\begin{aligned} H^{m_s} &= H_0^{m_s} + H_1^{m_s} \\ &= \left(\Delta\left|m_s\right| - \gamma_e B_z m_s\right) - \sum_{\mathsf{j}} \omega_0 I_z^{\mathsf{j}} + m_s \sum_{n=x,y,z} \alpha_{zn}^{\mathsf{j}} I_n^{\mathsf{j}} + \sum_{\mathsf{j}>\mathsf{k}} \sum_{m,n=x,y,z} I_m^{\mathsf{j}} \tilde{\beta}_{mn}^{\mathsf{j},\mathsf{k}}\left(m_s\right) I_n^{\mathsf{k}} \end{aligned} \quad \text{(S7)}$$

where $\tilde{\beta}_{mn}^{\mathsf{j},\mathsf{k}}\left(m_s\right) = \beta_{mn}^{\mathsf{j},\mathsf{k}} + \delta\beta_{mn}^{\mathsf{j},\mathsf{k}}\left(m_s\right)$ is the total coupling between the $\mathsf{j}-th$ and $\mathsf{k}-th$ nuclear spins.

For the $m_s = 0$ subspace, the effective Hamiltonian is

$$H_{nuc}^{m_s=0} = -\sum_{\mathsf{j}} \omega_0 I_z^{\mathsf{j}} + \sum_{\mathsf{j}>\mathsf{k}} \sum_{m,n=x,y,z} I_m^{\mathsf{j}} \tilde{\beta}_{mn}^{\mathsf{j},\mathsf{k}}\left(0\right) I_n^{\mathsf{k}}. \quad \text{(S8)}$$

When the Zeeman splitting is large (i.e., $\omega_0 \gg \tilde{\beta}_{mn}^{\mathsf{j},\mathsf{k}}\left(0\right)$), we neglect the non-secular terms of $\delta\beta$ and obtain the simplified Hamiltonian for $m_s = 0$:

$$H_{nuc}^{m_s=0} \approx -\sum_{\mathsf{j}} \omega_0 I_z^{\mathsf{j}} + \sum_{\mathsf{j}>\mathsf{k}} I_z^{\mathsf{j}} \tilde{\beta}_{zz}^{\mathsf{j},\mathsf{k}}\left(0\right) I_z^{\mathsf{k}} + \sum_{\mathsf{j}>\mathsf{k}} \left(b^{\mathsf{j},\mathsf{k}} I_+^{\mathsf{j}} I_-^{\mathsf{k}} + \left(b^{\mathsf{j},\mathsf{k}}\right)^* I_-^{\mathsf{j}} I_+^{\mathsf{k}} \right), \quad \text{(S9)}$$

where $b^{\mathsf{j},\mathsf{k}} = \frac{1}{4}\left(\tilde{\beta}_{xx}^{\mathsf{j},\mathsf{k}} + \tilde{\beta}_{yy}^{\mathsf{j},\mathsf{k}} + i\tilde{\beta}_{xy}^{\mathsf{j},\mathsf{k}} - i\tilde{\beta}_{yx}^{\mathsf{j},\mathsf{k}}\right)$. Both Ising coupling and flip-flop coupling may exist for the $m_s = 0$ subspace.

For the $m_s = 1$ subspace, the effective Hamiltonian is

$$H_{nuc}^{m_s=1} = -\sum_{\mathsf{j}} \omega_0 I_z^{\mathsf{j}} + \sum_{n=x,y,z} \alpha_{zn}^{\mathsf{j}} I_n^{\mathsf{j}} + \sum_{\mathsf{j}>\mathsf{k}} \sum_{m,n=x,y,z} I_m^{\mathsf{j}} \tilde{\beta}_{mn}^{\mathsf{j},\mathsf{k}}\left(1\right) I_n^{\mathsf{k}}. \quad \text{(S10)}$$

where we have dropped the constant $\Delta - \gamma_e B_z$ term for simplicity. The first two terms imply that the j-th nuclear spin precesses around the vector $\vec{\omega}^{\mathsf{j}} \equiv -\omega_0 \vec{e}_z + \sum_{n=x,y,z} \alpha_{zn}^{\mathsf{j}} \vec{e}_n$, and the quantization axis is $\vec{e}_z^{\mathsf{j}} \equiv \vec{\omega}^{\mathsf{j}} / \left|\vec{\omega}^{\mathsf{j}}\right|$. When the hyperfine interactions are sufficiently different $\left|\vec{\omega}^{\mathsf{j}} - \vec{\omega}^{\mathsf{k}}\right| \gg \tilde{\beta}_{mn}^{\mathsf{j},\mathsf{k}}\left(1\right)$, all couplings between the nuclear spins are suppressed except for the Ising coupling. The simplified Hamitonian for $m_s = 1$ is:

$$H_{nuc}^{m_s=1} \approx \sum_{\mathsf{j}} \left|\vec{\omega}^{\mathsf{j}}\right| I_{z_{\mathsf{j}}}^{\mathsf{j}} + \sum_{\mathsf{j}>\mathsf{k}} I_{z_{\mathsf{j}}}^{\mathsf{j}} \tilde{\beta}_{z_{\mathsf{j}} z_{\mathsf{k}}}^{\mathsf{j},\mathsf{k}}\left(1\right) I_{z_{\mathsf{k}}}^{\mathsf{k}}, \quad \text{(S11)}$$

where $\tilde{\beta}^{\mathsf{j},\mathsf{k}}_{z_{\mathsf{j}}z_{\mathsf{k}}}(1) = \sum_{m,n=x,y,z} \left(\vec{e}^{\mathsf{j}}_z\right)_m \cdot \tilde{\beta}^{\mathsf{j},\mathsf{k}}_{mn}(1) \cdot \left(\vec{e}^{\mathsf{k}}_z\right)_m$. For example, with only two proximal nuclear spins $\mathbf{n}_1$ and $\mathbf{n}_2$, and $|\vec{\omega}^1 - \vec{\omega}^2| \gg \tilde{\beta}^{1,2}_{mn}(1)$,

$$H^{m_s=1}_{nuc} \approx \left|\vec{\omega}^1\right| I^1_{z_1} + \left|\vec{\omega}^2\right| I^2_{z_2} + I^1_{z_1} \tilde{\beta}^{1,2}_{z_1 z_2}(1)\, I^2_{z_2}. \tag{S12}$$

If spin $\mathbf{n}_2$ is in the completely mixed state, then spin $\mathbf{n}_1$ has two possible energy splittings $|\vec{\omega}^1| \pm \frac{1}{2}\tilde{\beta}^{1,2}_{z_1 z_2}(1)$. With a nuclear spin Ramsey experiment (Fig. S2), we should be able to either resolve such energy splitting (by observing the beating at frequency $\tilde{\beta}^{1,2}_{z_1 z_2}(1)$) or give an upper bound on the magnitude of $\tilde{\beta}^{1,2}_{z_1 z_2}(1)$.

S.2.3. Hyperfine Coupling for the First Nuclear Spin

We now justify the claim that spin $\mathbf{n}_1$ has approximately the same quantization axis for both $m_s = 0$ and $m_s = 1$ subspaces. Since the static magnetic field is along the NV axis $\vec{B} = B_z \vec{e}_z$, there is no enhancement from the g-tensor. Considering only one nuclear spin $\mathbf{n}_1$, we may reduce Eq. (S7) to

$$H^{1,m_s} = -\omega_0 I^1_z + m_s \sum_n \alpha^1_{zn} I^1_n \tag{S13}$$

For the $m_s = 0$ subspace, spin $\mathbf{n}_1$ has the quantization axis $\hat{n}_{m_s=0} = \vec{e}_z$. For $m_s = 1$ subspace, we may calculate the quantization axis $\hat{n}_{m_s=1}$ using the hyperfine tensor $\alpha^{(1)}_{mn}$ associated with spin $\mathbf{n}_1$.

If the hyperfine coupling is due to the contact interaction that is isotropic, the hyperfine tensor is proportional to the identity matrix, $\alpha^1_{mn} \propto \delta_{mn}$, and the relevant Hamiltonian can be reduced to $-\mu_n B_z I^1_z + S_z \alpha^1_{zz} I^1_z$. This implies that the quantization axis $\hat{n}_{m_s=1} = \vec{e}_z$ is also along the NV axis. If the hyperfine coupling also contains a dipolar interaction that is anisotropic, the hyperfine tensor can be characterized by three principle axes with associated principle values. If one of the principle axis is fairly close to the NV axis and the three principle values are also quite similar, then the quantization axis of $\mathbf{n}_1$ can be still very close to the NV axis.

The hyperfine tensors have be calculated with density functional theory (DFT) [*S5*] and obtained from the CW ensemble EPR spectra measurements [*S7*]. In our experiment, we can measured the projection of the hyperfine tensor along the NV axis

$$\alpha^1_z \equiv \left|\alpha^1_{zx}\vec{e}_x + \alpha^1_{zy}\vec{e}_y + \alpha^1_{zz}\vec{e}_z\right| = \sqrt{\left(\alpha^1_{zx}\right)^2 + \left(\alpha^1_{zy}\right)^2 + \left(\alpha^1_{zz}\right)^2}. \tag{S14}$$

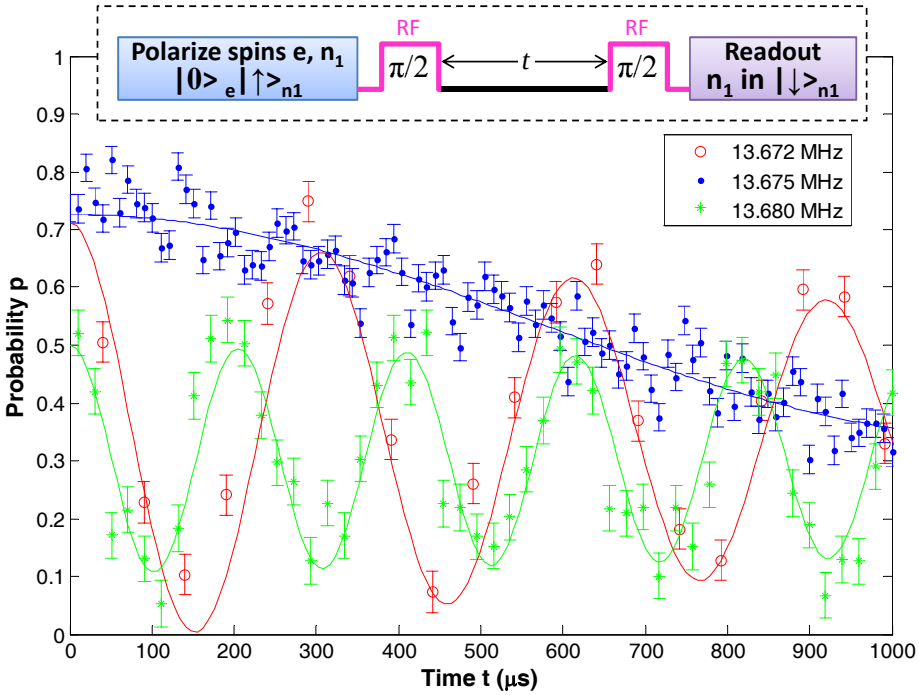

Figure S2: Ramsey fringes for the nuclear spin $\mathbf{n}_1$. The operations for the nuclear Ramsey experiment are given in the dashed box. Three difference frequencies $\nu = 13.672, 13.675$, and 13.680 MHz are used for the RF field. The frequency for the Ramsey fringes is determined by the detuning of the RF field $\nu - \nu_0$, where $\nu_0 = 13.675\,(1)$ MHz. There is no significant decay in the amplitude of the Ramsey fringes up to 1 ms.

We perform a Ramsey experiment for spin $\mathbf{n}_1$ in $m_s = 1$ subspace, which measures the level splitting between $|1\rangle_e\,|\downarrow\rangle_{n1}$ and $|1\rangle_e\,|\uparrow\rangle_{n1}$ to be $13.675\,(1)$ MHz (see Fig. S2). This value also includes $\omega_0 = \pm 32\,(1)$ kHz contribution of Zeeman splitting due to 30 gauss magnetic field parallel/antiparallel to the NV axis [*S4*]. Thus, the projection of the hyperfine tensor along the NV axis is $\alpha_z^1 = 13.675\,(1) \pm 0.032\,(1)$ MHz. The measured values match those reported by Felton et al. in bulk ESR studies [*S7*]. The reported hyperfine tensor implies that the quantization axis $\hat{n}_{m_s=1} = \sin\delta\ \vec{e}_x + \cos\delta\ \vec{e}_z$ for $|m_s = 1\rangle_e$, where $\delta = \arctan\frac{\alpha_{xz}^1}{\alpha_{zz}^1} \approx 6.7^\circ$ is

the angle between $\hat{n}_{m_s=0}$ and $\hat{n}_{m_s=1}$. Thus, the nuclear spin eigenstates for $m_s = 1$ subspace differ from the nuclear spin eigenstates for $m_s = 1$ subspace by a small angle δ. The difference between these two state is $\sin^2\delta \approx 0.007$, which is too small to be resolved with the current precision. Therefore, with our measurement precession, we have justified to claim that the quantization axis of the nuclear spin $\mathbf{n}_1$ almost does not depend on the electronic spin state $|m_s = 0\rangle_e$ or $|m_s = 1\rangle_e$. We may use the simple notation of $|0\rangle_e |\downarrow\rangle_{n1}, |0\rangle_e |\uparrow\rangle_{n1}, |1\rangle_e |\downarrow\rangle_{n1}$, and $|1\rangle_e |\uparrow\rangle_{n1}$ provides a good approximation for the eigenstates of the Hamiltonian in Eq. (S13).

S.2.4. Spin Flip-Flop Interaction between Nuclear Spins

We now consider the interaction between two nuclear spins $\mathbf{n}_1$ and $\mathbf{n}_2$. According to Eq. (S9), the effective secular spin Hamiltonian between spins $\mathbf{n}_1$ and $\mathbf{n}_2$ for $m_s = 0$ subspace is

$$H_{nuc}^{m_s=0} = \omega_0 I_z^1 + \omega_0 I_z^2 + \tilde{\beta}_{zz}^{1,2} I_1^1 I_z^2 + b^{1,2}(I_+^1 I_-^2 + I_-^1 I_+^2),$$

where we choose $b^{1,2}$ real by absorbing the complex phase into I_+^1. Experimentally, we estimate $\tilde{\beta}_{zz}^{1,2} \lesssim 0.3$ kHz from the nuclear spin Ramsey experiment (as the Ramsey fringes can be observed even up to 3 ms (Fig. S2)), which is one or two orders of magnitude smaller than $b^{1,2} = 4.27\,(3)$ kHz or $\omega_0 = 32\,(2)$ kHz, which corresponds to magnetic field of ~ 30 gauss. The observation is also consistent with the theoretical estimate from the hyperfine tensors [*S14*]. For simplicity, we will neglect the $\tilde{\beta}_{zz}^{1,2}$ term and consider the following Hamiltonian:

$$H_f = \omega_0 \left(I_z^1 + I_z^2\right) + b(I_+^1 I_-^2 + I_-^1 I_+^2), \tag{S15}$$

where $b = b^{1,2} = \left|\frac{1}{4}\left(\tilde{\beta}_{xx}^{1,2} + \tilde{\beta}_{yy}^{1,2} + i\tilde{\beta}_{xy}^{1,2} - i\tilde{\beta}_{yx}^{1,2}\right)\right|$. Neglecting $\tilde{\beta}_{zz}^{1,2}$ may introduce an error with probability $\left(\tilde{\beta}_{zz}^{1,2}/b\right)^2 \lesssim 1\%$, which is actually small compared to other imperfections. In principle, we may also use quantum control techniques [*S8*] to completely compensate the deviation due to finite $\tilde{\beta}_{zz}^{1,2}$.

The nuclear spins $\mathbf{n}_1$ and $\mathbf{n}_2$ have initial poalrization $p_{n_1} \equiv p_{n_1,\uparrow} - p_{n_1,\downarrow}$ and $p_{n_2} \equiv p_{n_2,\uparrow} - p_{n_2,\downarrow}$, respectively. The initial densitiy matrix of the two nuclear spins is $\rho_0 = \rho_{10} \otimes \rho_{20}$, with $\rho_{10} = \frac{1}{2}(1 + p_{n_1} I_z^1)$ and $\rho_{20} = \frac{1}{2}(1 + p_{n_2} I_z^2)$. The evolution of the density matrix of spin $\mathbf{n}_1$ is

$$\rho_1(\tau) = \mathtt{Tr}_{\mathbf{n_2}}\{U\rho_0 U^\dagger\} = \frac{1}{2} + I_z^1(p_{n_1} + (p_{n_2} - p_{n_1})\sin^2 b\tau), \tag{S16}$$

where $U = \exp(-iH_f\tau)$ is the evolution operator and $\mathtt{Tr}_{\mathbf{n}_2}$ traces out the subsystem of spin $\mathbf{n}_2$. Therefore, the polarization of spin $\mathbf{n}_1$ can be written as

$$p_{n_1}(\tau) = p_{n_1} + (p_{n_2} - p_{n_1}) \sin^2 b\tau. \tag{S17}$$

We observe that when the two nuclei are polarized equally ($p_{n_1} = p_{n_2}$) and $p_{n_1} \neq 0$, there is no flip-flop between them. For example, consider the two nuclei prepared in either $\uparrow\uparrow$ or $\downarrow\downarrow$. In this case, flip-flops are suppressed because of the energy gap ($2\omega_0 \gg b$) between the $\uparrow\uparrow$ and $\downarrow\downarrow$ configurations. On the other hand, when both nuclei are prepared with opposite polarizations ($p_{n_1} = -p_{n_2}$), the spin flip-flops are maximized since the energy gap between $\uparrow\downarrow$ and $\downarrow\uparrow$ is near zero. After a time of $\tau = \pi/2b$, the $\uparrow\downarrow$ part has evolved to $\downarrow\uparrow$ (i.e., the SWAP operation).

Meanwhile, for $m_s = 1$ subspace, the two nuclear spins have very different energy splittings due to the distinct hyperfine couplings (see the discussion after Eq. (S10)). This would suppress the spin flip-flop terms. As shown in Fig. S3, the flip-flop process between spins $\mathbf{n}_1$ and $\mathbf{n}_2$ are significantly suppressed when the electronic spin is $|m_s = 1\rangle_e$. The residual oscillations are due to the imperfect preparation of the electronic spin (e.g., optical pumping and π pulses) that induces a small probability in $m_s = 0$.

We can use the oscillation amplitudes for both $m_s = 0$ and $m_s = 1$ subspaces to estimate the polarization of the electronic spin after optical pumping. Suppose the polarization of the electronic spin is $1 - \varepsilon_{pump}$, the ratio of two oscillation amplitudes is approximately $\frac{A_{m_s=1}}{A_{m_s=0}} \approx \frac{\frac{\varepsilon_{pump}}{2} + \varepsilon_{MW}}{1 - \varepsilon_{pump}}$, where the total error probability associated with MW π-pulses is $\varepsilon^{MW} = \varepsilon^{MW}_{\text{res}} + \varepsilon^{MW}_{\text{det}} \approx 0.08$. Thus, we estimate $\varepsilon_{pump} \approx 0.16 \pm 0.07$. This estimate of spin polarization is consistent with that found by Harrison et. al. [*S9*] who studied optical spin polarization in ensembles of NV centers at cryogenic temperature using ESR spectroscopy.

S.3. NUCLEAR SPIN DEPOLARIZATION FOR EACH READOUT

The mechanism for depolarization of nuclear spins under optical illumination is induced by stochastic electronic optical transitions, which connect multiple electronic states with different hyperfine interactions to the nuclear spins [*S10*, *S11*]. The process can described by the master equation that accounts for both the classical stochastic transition of the electronic states and the coherent evolution of the nuclear spins with state-dependent hyperfine

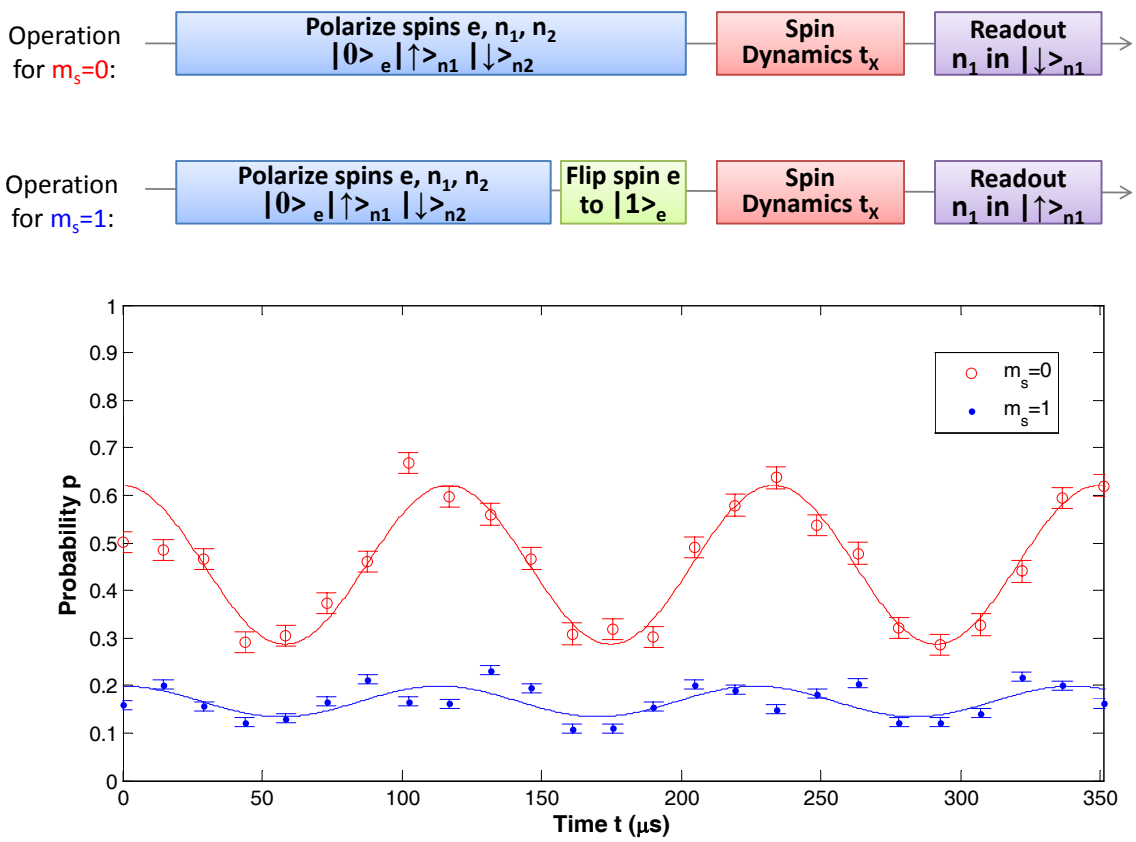

Figure S3: Dynamics of nuclear spins for $m_s = 0$ and $m_s = 1$ subspaces. The nuclear spins $\mathbf{n}_1$ and $\mathbf{n}_2$ are initialized in $|\uparrow\rangle_{n_1}|\downarrow\rangle_{n_2}$. When the electronic spin is $|m_s = 0\rangle_e$, there is a flip-flop process between the two nuclear spins (red curve). When the electronic spin is $|m_s = 1\rangle_e$, the flip-flop process is strongly suppressed (blue curve).

interactions. For fast optical excitation/relaxation, the evolution under each of these different hyperfine interactions is suppressed. This increases the depolarization time for the nuclear spin.

Reducing the transverse magnetic field with respective to the NV axis can further increase the depolarization time of the nuclear spin [*S10*, *S11*]. The theoretical description for the depolarization of the nuclear spin under optical illumination is detailed in [*S10*]. The same theoretical model can also explain the observed double exponential decay in Fig. 2D, which is associated with the two time scales for dephasing and depolarizing with respective to the

motional-averaged quantization axis [*S10*].

Since the power for the laser pulses is almost the same for the experiments presented in Figures 2, 3,and 4, we may use the depolarization curve (Fig. 2D) to estimate the relative reduction in polarization for various operations. For the first nuclear spin, the relative reduction of polarization ε_{n1} is 0.035 ± 0.015 after each 350 ns green laser pulse. For the second nuclear spin, we estimate the relative reduction of polarization ε_{n2} is about 0.3 ± 0.1 after 5 μs green laser pulse, and about 0.5 ± 0.1 after 20 μs green laser pulse.

Note also that the imperfect optical pumping of the electronic spin can be made very small with sufficiently long optical pulse, but this is not optimal for our repetitive readout scheme, because long optical illumination eventually induces depolarization of the nuclear spins that store useful information. To mitigate the perturbation to the nuclear spins, 350 ns green optical pumping pulses are chosen that result in 75% electronic spin polarization in the state $|0\rangle_e$. This affects all readouts immediately proceeded by an optical readout pulse (i.e., $m = 2, \cdots, M$), which degrades the gain in signal amplitude. These effects are estimated through numerical simulations of the repeated readout scheme in the following sections.

S.4. DERIVING OPTIMIZED SNR

The rate of optical fluorescence of the NV center depends strongly on the electronic spin state for up to 500 ns after the center is optically probed at wavelengths below the zero-phonon line [*S1*]. We define $\overline{n^0}$ and $\overline{n^1}$ as the average number of photons detected during a 325 ns measurement interval (i.e. readout) for the $|0\rangle_e$ and $|1\rangle_e$ states respectively. For a set of repeated readouts, we obtain the average number of counts $\overline{n_m}(\{p\})$ where the bar indicates the average number of photons over N experimental realizations and the m subscript indexes the repeated readout. The $\{p\}$ represent controllable parameters of the experiment. For example in a Rabi experiment $p = t_p$, the duration of microwave radiation.

We extract the signal amplitudes A_m for the mth measurement interval by fitting each $\overline{n}_m(t_p)$ readout of a Rabi experiment to a cosine curve of the form: $A_m \cos(\Omega_{MW} t_p) + B_m$. The value A_0 is the amplitude of a Rabi oscillation with full initial spin polarization (Fig. 1B of the main text). The standard error $\overline{\sigma}_m$ of the mth measurement is found to be almost independent of m: $\sigma_m \approx \sigma_0$, with σ_0 being the uncertainty associated with the measurement

of A_0. Since the $|A_m|$ values decrease with increasing m (Fig. 3D of main text), it is optimal to weight each element of the measurement record.

We use the signal-to-noise ratio (SNR) as the figure of merit for the repetitive readout scheme. The signal is defined as the weighted sum of the Rabi oscillation amplitudes obtained from repetitive readout.

$$\text{Signal} = \sum_{m=1}^{M} w_m \left|A_m\right|, \tag{S18}$$

with weight w_m for the m-th readout. The corresponding noise is

$$\text{Noise} = \sqrt{\sum_{m=1}^{M} w_m^2 \sigma_m^2}, \tag{S19}$$

where σ_m is the noise for the m-th readout, which can also be obtained experimentally. The signal-to-noise ratio [*S12*] is defined as

$$\frac{\text{Signal}}{\text{Noise}} = \frac{\sum_{m=1}^{M} w_m \left|A_m\right|}{\sqrt{\sum_{m=1}^{M} w_m^2 \sigma_m^2}}. \tag{S20}$$

According to the Cauchy-Schwartz inequality, we have

$$\sum_{m=1}^{M} \left(w_m \sigma_m\right)^2 \sum_{m=1}^{M} \left(\frac{\left|A_m\right|}{\sigma_m}\right)^2 \geq \left(\sum_{m=1}^{M} w_m \left|A_m\right|\right)^2, \tag{S21}$$

where equality is satisfied when $w_m = \left|A_m\right| / \sigma_m^2$. Therefore, the optimized SNR is

$$\text{SNR}_{\text{opt}}\left(M\right) = \sqrt{\sum_{m=1}^{M} \left|\frac{A_m}{\sigma_m}\right|^2}. \tag{S22}$$

In Figure S4, we plot the SNR curves for optimal weighting and for equal weighting of each measurement for the single proximal nuclear spin repeated readout. We see that for the equal weighting case, after $M \approx 20$ the SNR begins to degrade. This is because of the reduction of the signal amplitude A_m for increasing m due to nuclear spin depolarization, while the noise level σ_m remains almost constant. The weighting factors w_m allow for updating the measurement records to most efficiently use the information with respect to the noise.

S.5. SIMULATION FOR THE REPETITIVE READOUT

We have performed a numerical simulation for both repetitive readout schemes. We use the transition matrix description to keep track of the state evolution. With reasonable choice

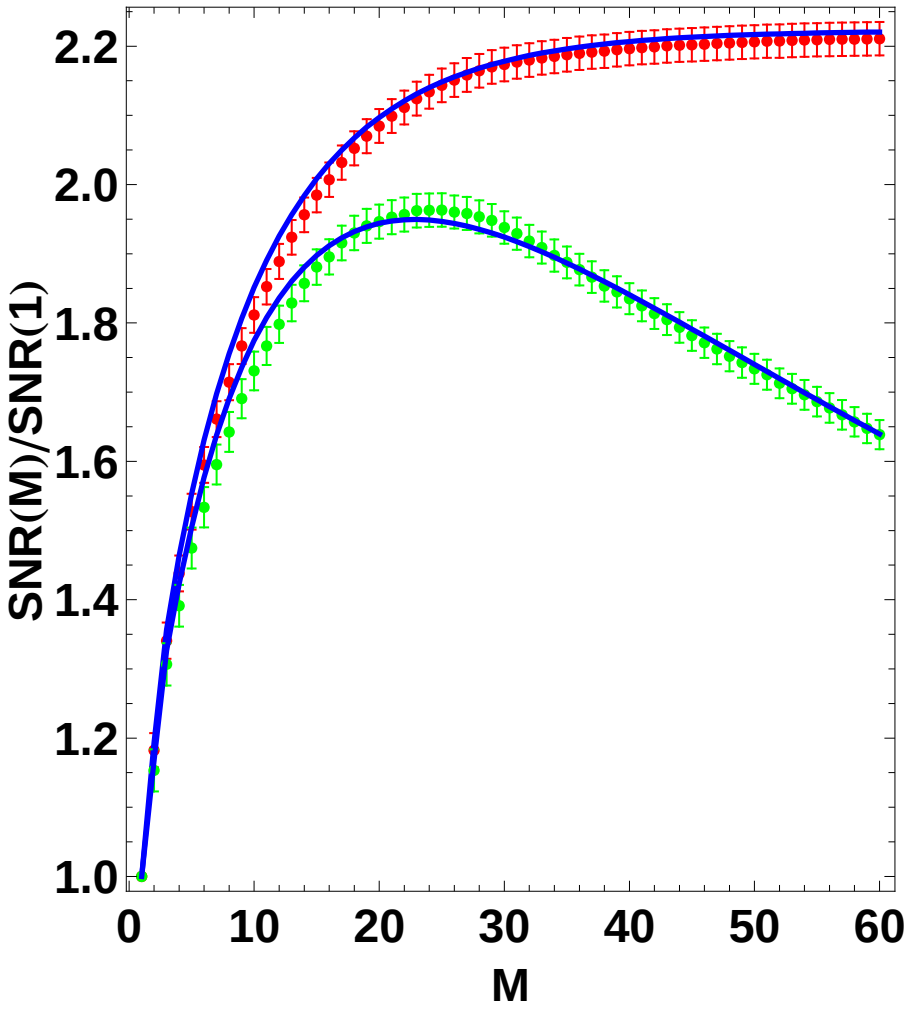

Figure S4: Signal-to-Noise ratio for repetitive readout. The green data points correspond to the SNR where $w_m = 1$ for all measurements of the A_m amplitudes and σ_m uncertainties. The red data are for the optimized SNR values where $w_m = |A_m|/\sigma_m^2$ and reach the best SNR improvement of 220%. The blue curves are the theoretical fits to our model for measurement of the NV center electronic spin and fit well to the data. Note that the model is identical for both cases.

of imperfection parameters, we are able to obtain A_m and $\mathrm{SNR}_{\mathrm{opt}}(M)$ consistent with the experiment.

S.5.1. Transition matrices

We model $8 = 2^3$ levels associated with the electronic spin and two nuclear spins in the simulation. Because the quantum coherence does not change the outcome of the repetitive

readout, it is sufficient to track the probability distribution over these 8 levels. We use the array $\vec{q} = (q_{0\downarrow\downarrow}, q_{0\downarrow\uparrow}, q_{0\uparrow\downarrow}, q_{0\uparrow\uparrow}, q_{1\downarrow\downarrow}, q_{1\downarrow\uparrow}, q_{1\uparrow\downarrow}, q_{1\uparrow\uparrow})^T$ to represent the probability distribution. We consider the transition matrices for various operations characterized by imperfection parameters. For example, if initial state distribution is $\vec{q}_0$ and transition matrix is $\mathcal{T}$, the final state distribution is $\mathcal{T}\vec{q}_0$.

We now list the transition matrices for the operations that are used for spin initialization and repetitive readout.

1) Transition matrix for MW1 π-pulse is

$$\mathcal{T}_{\rm MW1} = W_{pi} \otimes I_\downarrow \otimes \mathbb{1}_2 + W_{id} \otimes I_\uparrow \otimes \mathbb{1}_2, \tag{S23}$$

where

$$W_{pi} = \begin{pmatrix} \varepsilon_{\rm res}^{MW} & 1-\varepsilon_{\rm res}^{MW} \\ 1-\varepsilon_{\rm res}^{MW} & \varepsilon_{\rm res}^{MW} \end{pmatrix} \qquad W_{id} = \begin{pmatrix} 1-\varepsilon_{\rm det}^{MW} & \varepsilon_{\rm det}^{MW} \\ \varepsilon_{\rm det}^{MW} & 1-\varepsilon_{\rm det}^{MW} \end{pmatrix}$$

$$I_\downarrow = \begin{pmatrix} 1 & 0 \\ 0 & 0 \end{pmatrix} \qquad I_\uparrow = \begin{pmatrix} 0 & 0 \\ 0 & 1 \end{pmatrix} \qquad \mathbb{1}_2 = \begin{pmatrix} 1 & 0 \\ 0 & 1 \end{pmatrix}$$

with $\varepsilon_{\rm res}^{MW} = 0.07$ for the resonant transition and $\varepsilon_{\rm det}^{MW} = 0.01$ for the Δ-detuned transition (see Sec. I C). Similarly the transition matrix for MW2 π-pulse is

$$\mathcal{T}_{\rm MW2} = W_{pi} \otimes I_\uparrow \otimes \mathbb{1}_2 + W_{id} \otimes I_\downarrow \otimes \mathbb{1}_2. \tag{S24}$$

2) The transition matrices for nuclear spin depolarization under optical illumination are

$$\mathcal{T}_{n1} = \mathbb{1}_2 \otimes \begin{pmatrix} 1-\frac{\varepsilon_{n1}}{2} & \frac{\varepsilon_{n1}}{2} \\ \frac{\varepsilon_{n1}}{2} & 1-\frac{\varepsilon_{n1}}{2} \end{pmatrix} \otimes \mathbb{1}_2 \tag{S25}$$

for $\mathbf{n}_1$, and

$$\mathcal{T}_{n2} = \mathbb{1}_2 \otimes \mathbb{1}_2 \otimes \begin{pmatrix} 1-\frac{\varepsilon_{n1}}{2} & \frac{\varepsilon_{n1}}{2} \\ \frac{\varepsilon_{n1}}{2} & 1-\frac{\varepsilon_{n1}}{2} \end{pmatrix} \tag{S26}$$

for $\mathbf{n}_2$. The depolarization factors are $\varepsilon_{n1} = 0.05$ for $\mathbf{n}_1$ after $t_{green} = 350$ ns green laser pulse, and $\varepsilon_{n2} = 0.42$ and 0.63 for the second nuclear spin after 5 and 20 μs green laser pulses (see Sec. III). During the M-step repetitive readout, the flip-flop evolution between $\mathbf{n}_1$ and

$\mathbf{n}_2$ during the short 1.5 μs interval between sequential readouts may occur with probability about 5%, which is also effectively included into ε_{n2}.

3) The transition matrix for optical pumping of the electronic spin is

$$\mathcal{T}_{\mathrm{Pump}} = \begin{pmatrix} 1-\varepsilon_{pump,0} & 1-\varepsilon_{pump,1} \\ \varepsilon_{pump,0} & \varepsilon_{pump,1} \end{pmatrix} \otimes \mathbb{1}_2 \otimes \mathbb{1}_2, \tag{S27}$$

where $\varepsilon_{pump,0}$ and $\varepsilon_{pump,1}$ are the error probability for imperfect pumping. The characteristic time for optical pumping of the electronic spin is $\tau_{pump} = 235$ ns, so the 350 ns green laser pulse has $\varepsilon_{pump,1} = 0.25$. In addition, we also assume that there will be $\varepsilon_{pump,0} = 2\%$ of the population from $m = 0$ to $m = 1$ state.

4) The transition matrix for the RF π-pulse is

$$\mathcal{T}_{\mathrm{RF}} =_2 \otimes \begin{pmatrix} 1-\varepsilon_{RF} & \varepsilon_{RF} \\ \varepsilon_{RF} & 1-\varepsilon_{RF} \end{pmatrix} \otimes \mathbb{1}_2 \tag{S28}$$

where $\varepsilon_{RF} < 1\%$ based on our calibration, so we assume perfect RF π-pulse (i.e., $\varepsilon_{RF} = 0$) for simplicity. Similarly we also assume negligible error for the SWAP gate on $\mathbf{n}_1$ and $\mathbf{n}_2$.

S.5.2. Simulation with transition matrices

Using the above transition matrices, we can obtain the evolution in probability distribution for a given pulse sequence. For example, the distribution after k-step repeated pumping of $\mathbf{n}_1$ is

$$\vec{q}_k = \left(\mathcal{T}_{\mathrm{Pump}}\mathcal{T}_{\mathrm{RF}}\mathcal{T}_{\mathrm{MW2}}\right)^k \ \vec{q}_0, \tag{S29}$$

where $\vec{q}_0$ is the initial distribution. With these parameters, we first simulate and obtain the amplitude of nuclear Rabi oscillation, with amplitude 0.61, consistent with experimental observation of 0.60 ± 0.05.

For the pulse sequence provided in Fig. 3B of the main text, the state for the first readout is

$$\vec{q}^{(\delta)}_{\mathrm{meas},1} = \mathcal{T}_{\mathrm{RF}} \left(\mathcal{T}_{\mathrm{MW1}}\right)^{\delta} \ \vec{q}_{k=6}, \tag{S30}$$

where $\delta = 0$ for trivial MW1 pulse with duration $t = 0$, and $\delta = 1$ for MW1 π-pulse with duration $t = \pi/\Omega_{MW}$. The population difference in $|0\rangle_e$ between $\vec{q}^{(0)}_{\mathrm{meas},1}$ and $\vec{q}^{(1)}_{\mathrm{meas},1}$ gives the normalized amplitude

$$|A_1| = \left|\mathrm{Prob}\left[\vec{q}^{(0)}_{\mathrm{meas},1}\right] - \mathrm{Prob}\left[\vec{q}^{(1)}_{\mathrm{meas},1}\right]\right|, \tag{S31}$$

where

$$\text{Prob}\left[\vec{q}\right] = q_{0\downarrow\downarrow} + q_{0\downarrow\uparrow} + q_{0\uparrow\downarrow} + q_{0\uparrow\uparrow} \tag{S32}$$

is the probability in the $|0\rangle_e$ state for distribution $\vec{q}$.

The state for the following readout is

$$\vec{q}^{(\delta)}_{\text{meas},m} = \begin{cases} \left(\mathcal{T}_{\text{Pump}}\mathcal{T}_{\text{MW2}}\right)\vec{q}^{(\delta)}_{\text{meas},m-1} & \text{for even } m \\ \left(\mathcal{T}_{\text{Pump}}\mathcal{T}_{\text{MW1}}\right)\vec{q}^{(\delta)}_{\text{meas},m-1} & \text{for odd } m \end{cases}, \tag{S33}$$

with $m = 2, 3, \cdots, M$. Finally, the normalized amplitude for the m-th readout is

$$|A_m| = \left|\text{Prob}\left[\vec{q}^{(0)}_{\text{meas},m}\right] - \text{Prob}\left[\vec{q}^{(1)}_{\text{meas},m}\right]\right|. \tag{S34}$$

And

$$\text{SNR}_{\text{opt}}\left(M\right) = \sqrt{\sum_{m=1}^{M}|A_m|^2}. \tag{S35}$$

The simulation of A_m and $\text{SNR}_{\text{opt}}\left(M\right)$ for the repetitive readout scheme assisted with one qubits are shown in Fig. 3DE. Similarly, we can also simulate A_m and $\text{SNR}_{\text{opt}}\left(M\right)$ measured for the repetitive readout scheme assisted with two qubits are shown in Fig. 4CD.

[S1] N. B. Manson, J. P. Harrison, and M. J. Sellars, Phys. Rev. B **74**, 104303 (2006).

[S2] E. A. Donley, T. P. Heavner, F. Levi, M. O. Tataw, and S. R. Jefferts, Rev. Sci. Instrum. **76**, 063112 (2005).

[S3] A. Abragam and B. Bleaney, *Electron paramagnetic resonance of transition ions* (Clarendon P., Oxford,, 1970).

[S4] L. Childress, M. V. G. Dutt, J. M. Taylor, A. S. Zibrov, F. Jelezko, J. Wrachtrup, P. R. Hemmer, and M. D. Lukin, Science **314**, 281 (2006).

[S5] A. Gali, M. Fyta, and E. Kaxiras, Phys. Rev. B **77**, 155206 (2008).

[S6] D. Yao and J. Shi, American Journal of Physics **68**, 278 (2000).

[S7] S. Felton, A. M. Edmonds, M. E. Newton, P. M. Martineau, D. Fisher, D. J. Twitchen, and J. M. Baker, Phys. Rev. B **79**, 075203 (2009).

[S8] N. Khaneja, T. Reiss, C. Kehlet, T. Schulte-Herbruggen, and S. J. Glaser, J. Magn. Reson. **172**, 296 (2005).

[S9] J. Harrison, M. Sellars, and N. Manson, Diamond and Related Materials **15**, 586 (2006).

[S10] L. Jiang, M. V. G. Dutt, E. Togan, L. Childress, P. Cappellaro, J. M. Taylor, and M. D. Lukin, Phys. Rev. Lett. **100**, 073001 (2008).

[S11] M. V. G. Dutt, L. Childress, L. Jiang, E. Togan, J. Maze, F. Jelezko, A. S. Zibrov, P. R. Hemmer, and M. D. Lukin, Science **316**, 1312 (2007).

[S12] J. Gambetta, W. A. Braff, A. Wallraff, S. M. Girvin, and R. J. Schoelkopf, Phys. Rev. A **76**, 012325 (2007).

[S13] Note that our earlier experiment [*S11*] explores a different regime, where the external magnetic field has a transverse component with respect to the NV axis. Because of the anisotropy of the g-tensor for proximal nuclear spins, the transverse component can be enhanced depending on the hyperfine interaction. Thus, the proximal nuclear spins can have very different quantization axes, and different effective Zeeman splittings as well [*S4*].

[S14] The hyperfine tensor for n_1 is almost diagonal, with off-diagonal matrix elements much less than the diagonal ones (e.g., $\alpha^1_{xz} \ll \alpha^1_{xx}, \alpha^1_{yy}, \alpha^1_{zz}$). This suggests that it is very likely that $\delta\beta^{1,2}_{zz} \ll \delta\beta^{1,2}_{xx}, \delta\beta^{1,2}_{yy}$ for the electron-mediated nuclear spin coupling between n_1 and n_2.